



An Infrared Census of DUST in Nearby Galaxies with *Spitzer* (DUSTiNGS). V. The Period–Luminosity Relation for Dusty Metal-poor AGB Stars

S. R. Goldman¹ , M. L. Boyer¹ , K. B. W. McQuinn^{2,3} , P. A. Whitelock^{4,5}, I. McDonald⁶, J. Th. van Loon⁷ , E. D. Skillman⁸ , R. D. Gehrz⁸ , A. Javadi⁹, G. C. Sloan^{1,10}, O. C. Jones¹¹ , M. A. T. Groenewegen¹², and J. W. Menzies⁴

¹Space Telescope Science Institute, 3700 San Martin Drive, Baltimore, MD 21218, USA; sgoldman@stsci.edu

²University of Texas at Austin, McDonald Observatory, 2515 Speedway, Stop C1402, Austin, TX 78712 USA

³Rutgers University, Department of Physics and Astronomy, 136 Frelinghuysen Road, Piscataway, NJ 08854, USA

⁴South African Astronomical Observatory, P.O. Box 9, 7935 Observatory, South Africa

⁵Department of Astronomy, University of Cape Town, 7701 Rondebosch, South Africa

⁶Jodrell Bank Centre for Astrophysics, Alan Turing Building, University of Manchester, M13 9PL, UK

⁷Lennard-Jones Laboratories, Keele University, ST5 5BG, UK

⁸Minnesota Institute for Astrophysics, School of Physics and Astronomy, 116 Church Street SE, University of Minnesota, Minneapolis, MN 55455, USA

⁹School of Astronomy, Institute for Research in Fundamental Sciences (IPM), P.O. Box 19395-5531, Tehran, Iran

¹⁰University of North Carolina Chapel Hill, Chapel Hill, NC 27599-3255, USA

¹¹UK Astronomy Technology Centre, Royal Observatory, Blackford Hill, Edinburgh EH9 3HJ, UK

¹²Koninklijke Sterrenwacht van België, Ringlaan 3, B-1180 Brussels, Belgium

Received 2019 January 31; revised 2019 February 14; accepted 2019 February 18; published 2019 May 23

Abstract

The survey for DUST in Nearby Galaxies with *Spitzer* (DUSTiNGS) has identified hundreds of candidate dust-producing asymptotic giant branch (AGB) stars in several nearby metal-poor galaxies. We have obtained multi-epoch follow-up observations for these candidates with the *Spitzer Space Telescope* and measured their infrared (IR) light curves. This has allowed us to confirm their AGB nature and investigate pulsation behavior at very low metallicity. We have obtained high-confidence pulsation periods for 88 sources in seven galaxies. We have confirmed DUSTiNGS variable star candidates with a 20% success rate and determined the pulsation properties of 19 sources already identified as thermally pulsing AGB stars. We find that the AGB pulsation properties are similar in all galaxies surveyed here, with no discernible difference between the DUSTiNGS galaxies (down to 1.4% solar metallicity; $[\text{Fe}/\text{H}] = -1.85$) and the far more metal-rich Magellanic Clouds (up to 50% solar metallicity; $[\text{Fe}/\text{H}] = -0.38$). These results strengthen the link between dust production and pulsation in AGB stars and establish the IR period–luminosity relation as a reliable tool ($\pm 4\%$) for determining distances to galaxies, regardless of metallicity.

Key words: galaxies: dwarf – galaxies: stellar content – infrared: stars – Local Group – stars: AGB and post-AGB – stars: carbon

Supporting material: figure set, machine-readable tables

1. Introduction

Variable stars on the asymptotic giant branch (AGB) are known to show a linear correlation between the logarithm of the period and luminosity (Gerasimovič 1928). This relationship reveals details about the stellar physics that drives AGB evolution and, like the period–luminosity (P – L) relationship for Cepheids and RR Lyrae, is a useful distance indicator. As such, the AGB P – L relationship has been studied extensively over the years (Feast et al. 1989; Hughes & Wood 1990; Ita et al. 2004a; Glass et al. 2009; Soszyński et al. 2009). Many of these studies focus only on Galactic and Magellanic AGB variables, since AGB stars are difficult to identify and resolve in more distant galaxies, mainly due to extinction by circumstellar dust that almost always accompanies large-amplitude pulsation. As a result, the properties of the AGB P – L relation are not well constrained at low metallicity, and some uncertainty remains regarding its usefulness as a distance indicator in metal-poor galaxies and/or metal-poor galaxy halos (Feast et al. 2002).

Strong AGB pulsations and dust production are known to be tightly linked (Lagadec & Zijlstra 2008; Sloan et al. 2016; McDonald et al. 2018; McDonald & Trabucchi 2019). As a star evolves through the AGB phase, the strength of the pulsations grows, which simultaneously levitates more material to large

circumstellar radii, where it condenses into dust. The AGB stars can be either oxygen-rich (M-type) or carbon-rich (carbon stars), producing silicate-rich and carbonaceous dust, respectively. The processes dictating the envelope chemistry are third dredge-up events (TDUs) and hot-bottom burning (HBB), which depend primarily on a star’s initial mass (see the reviews by Herwig 2005; Karakas & Lattanzio 2014) and metallicity. Carbon stars produce enough carbon internally that they can produce significant amounts of dust regardless of their initial metallicity (Sloan et al. 2012), while oxygen-rich stars require heavier elements (e.g., Fe, Mg, Al, Si), which must be produced by a previous generation of stars or the by-products of TDUs and HBB (e.g., Sloan et al. 2010; Bladh et al. 2015).

How AGB mass loss, dust production, and evolution are affected by metallicity is still unclear. Variability studies in the Large (LMC) and Small (SMC) Magellanic Clouds have produced large samples of long-period variables (LPVs), but these samples span a narrow range in metallicity. Additional works have discovered large samples of LPVs in globular clusters and smaller samples in nearby dwarf galaxies (see Section 1.3). Here we present the first large-scale IR survey of LPVs in nearby galaxies, reaching lower metallicity than ever before.

1.1. LPV Stars

The driving force behind AGB pulsations is poorly understood. While sources within the instability strip of the Hertzsprung–Russell (H-R) diagram (e.g., Cepheid variables or RR Lyrae stars) pulsate as a result of a gravity-opacity instability known as the κ -mechanism, the large convection cells within an AGB star would likely disrupt both spherical symmetry and this mechanism (Liljegren et al. 2018).

Red giants and supergiants (RSGs) and AGB stars can follow several sequences on the P – L diagram, often labeled A through E (Wood et al. 1999; Ita et al. 2004a).¹³ Many of the sources on these sequences pulsate in multiple modes, with secondary periods falling on the other sequences (see Trabucchi et al. 2018). The B and C' sequences are composed of red giant branch (RGB) and AGB first-overtone radial pulsators. The dusty and evolved AGB stars, or Mira variables, primarily lie along the fundamental mode (sequence I; Riebel et al. 2010), also known as sequence C (Wood et al. 1999); however, some ($\sim 30\%$) lie along sequence D, with pulsation periods between 500 and 2000 days. These have been referred to as long secondary periods (LSPs) yet are clearly the dominant mode in some evolved stars (Nicholls et al. 2009; Trabucchi et al. 2017); the sequence will be discussed further in Section 5.5.

1.2. Dust at Low Metallicity

As a result of their different masses, AGB stars can have considerably different lifetimes. The main-sequence lifetime of AGB progenitors (low- and intermediate-mass stars; 0.8 – $8 M_{\odot}$) is between 0.1 and 12 Gyr, after which they typically spend 20% of that time as red giants, $\sim 1\%$ as early-AGB stars, and $\sim 0.1\%$ as thermally pulsing AGB (TP-AGB) stars (Marigo et al. 2008, 2017; Javadi et al. 2011b, 2017). On the TP-AGB, these stars will produce the most dust and contribute the most mass back to the interstellar medium (ISM; see review by Höfner & Olofsson 2018). Recent works exploring the metallicity dependence of dust production in carbon stars have produced mixed results. A strong dependence was originally suggested by van Loon (2000) and corroborated by van Loon et al. (2005) and van Loon (2006), while McDonald et al. (2011) and Sloan et al. (2012, 2016) found little to no dependence. Nanni et al. (2013, 2014) and Ferrarotti & Gail (2006) gave estimates of the metallicity dependence of the dust production using theoretical models. Work within the Galaxy and the Magellanic Clouds has also allowed us to study the effect of metallicity on the mass loss of oxygen-rich AGB stars (van Loon 2000, 2006; Goldman et al. 2017), with the results showing little to no effect on the measured mass-loss rates.

The DUST in Nearby Galaxies with *Spitzer* survey (DUSTiNGS; Boyer et al. 2015b, hereafter Paper I) searched for dust-producing AGB stars in 50 nearby (< 1.5 Mpc) metal-poor ($-2.7 < [\text{Fe}/\text{H}] < -1.0$) dwarf galaxies using *Spitzer Space Telescope* (Werner et al. 2004; Gehrz et al. 2007) InfraRed Array Camera (IRAC; Fazio et al. 2004) channels 1 and 2. The survey discovered hundreds of candidate dust-producing AGB stars at metallicities as low as 0.6% solar and provided no evidence for a strong metallicity dependence in overall dust production (Boyer et al. 2015a, hereafter Paper II). Observations at wavelengths longer than $\lambda = 5 \mu\text{m}$, where thermal emission from circumstellar dust dominates the IR

spectral energy distribution (SED), will be required to confirm this. Boyer et al. (2017, hereafter Paper IV) identified 146 carbon- and oxygen-rich stars by exploiting the strength of the water features in M-type stars and the CN+C₂ features found in carbon stars. Though most (120) of these sources were classified as carbon-rich, 26 were identified as M-type. These observations showed that dust is produced by both carbon- and oxygen-rich AGB stars over the full metallicity range spanned by DUSTiNGS. This suggests that metal-poor high-mass AGB stars can produce dust as early as 30 Myr after forming (for a $10 M_{\odot}$ star), while lower-mass carbon stars form dust after roughly 0.3–3.6 Gyr (van Loon et al. 2005). Therefore, AGB stars are likely important contributors of dust in the early universe. This work also led to the discovery of a potential dust-producing super-AGB star in IC 10 with an assumed mass ~ 8 – $12 M_{\odot}$ and strong water absorption indicative of an AGB star. Super-AGB stars are more massive ($6 M_{\odot} \lesssim M \lesssim 9 M_{\odot}$) AGB stars that are capable of fusing carbon and developing a degenerate oxygen–neon core. There is evidence that they can be dusty (Javadi et al. 2013) and produce the ONeMg white dwarfs that are responsible for neon nova explosions (Evans & Gehrz 2012). These stars may also be capable of ending in an electron-capture supernova without developing an iron core like the observationally similar RSGs (Doherty et al. 2015). We did not detect variability in this source due to a lack of temporal coverage (two epochs).

1.3. Metal-poor LPV Samples

Much of the information known about metal-poor LPVs is from the Optical Gravitational Lensing Experiment (OGLE; Udalski et al. 1997), Massive Compact Halo Object (MACHO; Alcock et al. 1997), and *Spitzer* Surveying the Agents of a Galaxy's Evolution (SAGE; Meixner et al. 2006; Riebel et al. 2010; Gordon et al. 2011; Riebel et al. 2015) surveys, with a handful of surveys in other galaxies (shown in Table 1). While a large number of metal-rich samples exists (Huang et al. 2018; Yuan et al. 2018), the majority of the more metal-poor LPVs have been found in Leo I, NGC 185, NGC 147, and NGC 6822, galaxies only slightly more metal-poor than the SMC. The most metal-poor sources to date were found by McDonald et al. (2010), who discovered two sequence-D variables in the globular cluster M15 at $[\text{Fe}/\text{H}] = -2.37$ dex (Harris 1996), and Whitelock et al. (2018), who discovered three LPVs in the Sagittarius dwarf irregular galaxy (Sag DIG). The metallicity of Sag DIG has been measured in both stars using red giants ($[\text{Fe}/\text{H}] = -1.88^{+0.13}_{-0.09}$; Kirby et al. 2017) and isochrones ($[\text{Fe}/\text{H}] = -2.1$; Momany et al. 2002) and the gas ($12 + \log(\text{O}/\text{H}) = 7.26$ – 7.50 ; Skillman et al. 1989; Saviane et al. 2002). One of these LPVs in Sag DIG has a pulsation period of 950 days, indicating a very late stage of evolution, and was found to be oxygen-rich (Paper IV). Variables have also been detected in globular clusters (Clement et al. 2001; Feast et al. 2002; Lebzelter & Wood 2005). However, their low mass limits these sources to the lower regions of the P – L sequences.

It is difficult to study the P – L relation at lower metallicities because so few LPVs have been discovered in this regime. The DUSTiNGS survey initially identified several LPV candidates using two-epoch photometry. Here we follow up with additional epochs and provide a larger sample to populate the P – L diagram over a large metallicity range ($-1.27 > [\text{Fe}/\text{H}] > -1.85$). DUSTiNGS is the first large-scale IR survey to identify the dustiest evolved stars in these galaxies. These stars can be

¹³ These sequences have also been labeled as 1–4, D, and E (e.g., Riebel et al. 2010).

Table 1
Surveys of LPVs in Nearby Galaxies, Including This Work

Galaxy	d (Mpc)	[Fe/H]	$12 + \log(\text{O}/\text{H})$ (mag)	M_V (mag)	Number of Sources with High-confidence Fit Periods	Number from Previous Work	Previous Work Reference
And IX	0.77	-2.20 ± 0.20	...	-8.1 ± 1.1	0	...	
DDO 216	0.92	-1.40 ± 0.02	7.93 ± 0.13	-12.2 ± 0.2	5	...	
Fornax ^a	0.15	-0.99 ± 0.01	...	-13.4 ± 0.3	...	7	Whitlock et al. (2009)
IC 10	0.79	-1.28	8.19 ± 0.15	-15.0 ± 0.2	16	...	
IC 1613	0.76	-1.6 ± 0.20	7.62 ± 0.05	-15.2 ± 0.2	15	9	Menzies et al. (2015)
Leo I ^a	0.25	-1.43 ± 0.01	...	-12.0 ± 0.3	...	26	Menzies et al. (2010)
NGC 147	0.68	-1.1 ± 0.10	...	-14.6 ± 0.1	8	168	Lorenz et al. (2011)
NGC 185	0.62	-1.3 ± 0.10	...	-14.8 ± 0.1	29	419	Lorenz et al. (2011)
NGC 6822 ^a	0.46	-1.0 ± 0.5	...	-15.2 ± 0.2	...	50+	Whitlock (2012)
Phoenix ^a	0.42	-1.37 ± 0.2	...	-9.9 ± 0.4	...	1	Menzies et al. (2008)
Sag DIG	1.07	-2.1 ± 0.20	$7.26 - 7.50$	-11.5 ± 0.3	0	3	Whitlock et al. (2018)
Sculptor ^a	0.09	-1.68 ± 0.01	...	-11.1 ± 0.5	...	2	Menzies et al. (2011)
Sextans A	1.43	-1.85	7.54 ± 0.06	-14.3 ± 0.1	6	...	
Sextans B	1.43	-1.6	7.53 ± 0.05	-14.5 ± 0.2	0	...	
WLM	0.93	-1.27 ± 0.04	7.83 ± 0.06	-14.2 ± 0.1	9	...	

Note. Distances, [Fe/H], and M_V are from McConnachie (2012) and references therein; the metallicity for Sextans B is from Bellazzini et al. (2014). Kirby et al. (2017) also derived a higher metallicity for Sag DIG of $[\text{Fe}/\text{H}] = -1.88^{+0.13}_{-0.09}$, based on RGB star spectroscopy. The ISM gas-phase oxygen abundances ($12 + \log(\text{O}/\text{H})$) are from Mateo (1998), Lee et al. (2006), and Saviane et al. (2002). An alternative name for DDO 216 is Pegasus dwarf irregular.

^a Galaxies not analyzed in this work.

obscured in the near-IR and optical. Observing in the IR ensures that all of the prominent dust producers are detected.

2. Data and Observations

We construct light curves using 3.6 and 4.5 μm imaging data from the IRAC on board *Spitzer*, with a mix of programs from both the cryogenic and post-cryogenic phases. Data include new and archival observations from 2003 to 2017.

2.1. DUSTiNGS

The DUSTiNGS data include both the original Cycle 8 data obtained in 2011–2012 (PID: 80063) and data obtained during the Cycle 11 follow-up program (PID: 11041) in 2015–2016. Light curves are sparsely sampled owing to the spacing of the *Spitzer* visibility windows for the DUSTiNGS galaxies, which are roughly 4–6 weeks long. There are typically two windows each year, separated by approximately 6 months. The Cycle 8 program, described in Paper I, obtained two epochs, one in each visibility window. The Cycle 11 program obtained six additional epochs, with a pair of observations at the beginning and end of each of the three consecutive visibility windows. The cadence is illustrated in Figure 1.

2.2. Archival Data

By taking advantage of the rich archival history of the *Spitzer Space Telescope*, we have been able to use data from 11 observing programs (Table 2). Most of the archival data that we use here are from two programs.

SPIRITS—The *SPitzer* InfraRed Intensive Transients Survey (SPIRITS; Kasliwal et al. 2017) program (Cycles 10–12, PID: 10136, 11063) was aimed at discovering explosive transients, eruptive variables, and new IR events lacking optical counterparts. The SPIRITS targets include a few of the DUSTiNGS galaxies: IC 1613, NGC 147, NGC 185, Sextans A, and Sextans B. These observations were taken between the original DUSTiNGS epochs and the follow-up DUSTiNGS observations, filling a gap in our temporal coverage (Figure 1).

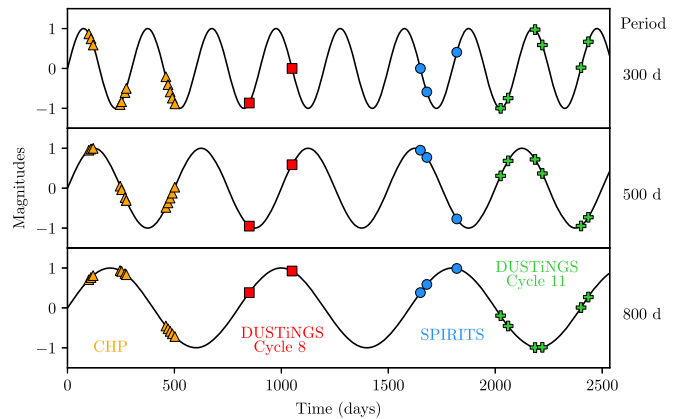


Figure 1. Artificial light curve showing the two initial DUSTiNGS observations (red) and six follow-up observations (green) fit with pulsation periods of 300, 500, and 800 days. Also shown is the cadence of the SPIRITS (blue) and CHP (orange) surveys; the cadence of the remaining archival programs is shown in Table 2.

Additional SPIRITS epochs cover the same epochs covered by the DUSTiNGS Cycle 11 observations and are included here.

The Carnegie Hubble Program—The Carnegie Hubble Program (CHP; Cycle 6, PID: 61001; Freedman et al. 2011) was aimed at determining distances to nearby galaxies using Cepheid variables. The CHP observations, taken between 2009 July and 2010 March, preceded both the DUSTiNGS and SPIRITS observations. The time between each epoch is ~ 10 days, given the focus on short-period variability (Figure 1).

We also use data from eight additional programs (individual observations are listed in Table 2) that sporadically sample the light curves between CHP and DUSTiNGS. The observations target 10 galaxies (listed in Table 1) that span a range in size ($-8.1 \text{ mag} > M_V > -15.2 \text{ mag}$), distance (0.62–1.43 Mpc), and, most notably, metal content ($-1.27 > [\text{Fe}/\text{H}] > -1.85$). We will use this range in metallicity to investigate its effect on the pulsation properties of evolved stars.

Table 2
The Archival *Spitzer* Observations

Galaxy	PID	AOR	R.A. (J2000)	Decl. (J2000)	Start Date (UT)	t_{exp} (hr)
IC 10	69	4424960	00 ^h 20 ^m 24 ^s .50	+59 ^d 17 ^m 30 ^s .0	2004 July 23	0.12
IC 10	61001	33204224	00 ^h 20 ^m 24 ^s .00	+59 ^d 18 ^m 14 ^s .0	2010 Jan 29	0.92
IC 10	61001	33203968	00 ^h 20 ^m 24 ^s .00	+59 ^d 18 ^m 14 ^s .0	2010 Feb 19	0.87
IC 10	61001	33203456	00 ^h 20 ^m 24 ^s .00	+59 ^d 18 ^m 14 ^s .0	2010 Mar 10	0.95
IC 10	61001	33202944	00 ^h 20 ^m 24 ^s .00	+59 ^d 18 ^m 14 ^s .0	2010 Sep 9	0.87
IC 10	61001	33202432	00 ^h 20 ^m 24 ^s .00	+59 ^d 18 ^m 14 ^s .0	2010 Oct 4	0.83
IC 10	61001	33201920	00 ^h 20 ^m 24 ^s .00	+59 ^d 18 ^m 14 ^s .0	2010 Oct 14	0.83
IC 1613	61001	33184000	01 ^h 04 ^m 58 ^s .20	+02 ^d 09 ^m 44 ^s .0	2010 Jan 26	0.97

Note. The full catalog ($n = 139$) is available for download in the electronic version and on VizieR. Information on the program IDs (PIDs) and individual observations (AORs) can be found through the *Spitzer* Heritage Archive.

(This table is available in its entirety in machine-readable form.)

3. Methods

3.1. PSF Photometry

We have point-spread function (PSF) photometry on all of the DUSTiNGS sources and archival data using the DUSTiNGS pipeline (described in Paper I). We performed PSF photometry using DAOPHOT II and ALLSTAR (Stetson 1987) on the coadded frames for the fainter sources ($[3.6] > 16$ mag) and individual frames for the brighter sources. For the fainter sources, mosaicked images were used to reduce Eddington bias (Eddington 1913) in sources near the detection threshold. A mosaicked and subsampled image can smear the PSF, for example, if it includes a rotation between frames. As a result, single frames were used for the brighter sources, which are more sensitive to changes in the PSF. For the photometry of our sample in IC 10, we have adjusted the magnitudes by 0.2 mag to account for foreground interstellar extinction (described further in Section 5.2). Paper I provides additional details on the photometry, saturation limits, photometric correction, and photometric completeness.

3.2. Identifying LPVs

The nonuniformity of the observing programs has resulted in varying depths and spatial coverage for each epoch. Therefore, many light curves are sparsely sampled. We have implemented the Lomb–Scargle algorithm (Lomb 1976; Scargle 1982) to determine the pulsation periods and amplitudes. The method fits a simple single-term sinusoidal light curve to different frequencies and then normalizes the results using the residuals. This method reduces the effects of unevenly spaced data using a more appropriate means of weighting within the Fourier transform (see review by VanderPlas 2018).

The nonuniform temporal and spatial coverage of the archival data has resulted in many sources with incomplete light curves from which we cannot derive reliable periods. To identify sources with sufficiently sampled light curves, we start by calculating the variability index (e.g., Gallart et al. 2004) that is defined as the ratio of the standard deviation of the measurements for a given star to the mean internal photometric uncertainty. A value of 1, 2, or 3 indicates variability at the 1σ , 2σ , or 3σ levels. We first restrict our light-curve fitting to stars with variability index > 1 . Second, we exclude sources with < 6 epochs from our light-curve analysis, a number that was also concluded as sufficient by Javadi et al. (2015). Finally, we restrict light-curve fitting to sources brighter than $M_{[3.6]} = -7.5$ mag, which includes all extreme

AGB (x-AGB) stars (Blum et al. 2006) in the LMC sample from Riebel et al. (2010). The x-AGB stars are the dustiest AGB stars that are likely in the superwind phase and very close to the end of their evolution. By restricting our sample to stars in the same brightness range as the LMC x-AGB stars, we limit contamination from fainter variable dusty objects, such as young stellar objects (YSOs) and background active galactic nuclei (AGNs).

3.3. Light-curve Analysis

For the sources that were included in the light-curve fitting, frequencies corresponding to 100–2000 days were fitted to each of the light curves using the Lomb–Scargle periodogram. Sources that were considered for further analysis were those that fit the following criteria.

1. A $[3.6]$ – $[4.5]$ color, of which the standard deviation did not deviate by more than 50% to eliminate sources that were not clearly dusty¹⁴ across epochs.
2. A best-fit solution where the peak frequency within the Fourier power spectrum was more than 6% higher than any other peak.
3. A best-fit solution constrained within a 95% confidence interval.

These three criteria determine which stars are included in further analysis. Stars excluded by these criteria are more likely to suffer from aliasing or poor data quality. The quality of the remaining sources was determined visually, with an eye for ensuring that the direction of brightness changes in the light curves matched the best-fit light curve, especially for short-term changes. The results of the light-curve fitting are shown in Table 3, which includes the midline magnitudes, fit periods and amplitudes for both 3.6 and 4.5 μm data, color properties, and classification confidence (described further below). An initial inspection of stars that pass these three criteria indicate that, at these distances, we are only able to reliably determine the pulsation periods of the dusty evolved sources using *Spitzer*.

Variations in spatial coverage between epochs caused some stars to be observed in only one of the filters, either $[3.6]$ or $[4.5]$. Some of these light curves can be augmented where $[3.6]$ data do not exist by including the 4.5 μm data and using the mean color to derive 3.6 μm magnitudes. This was done only if the color was determined to be stable ($\sigma_{[3.6]-[4.5]} < 20\%$) and

¹⁴ Sources that lacked 4.5 μm measurements were still included in the final categorization and analysis.

Table 3
The Results of 3.6 and 4.5 μm Light-curve Fitting

(1)	(2)	(3)	(4)	(5)	(6)	(7)	(8)	(9)	(10)	(11)	(12)	(13)	(14)
Galaxy	Target ID	R.A. (deg)	Decl. (deg)	(3.6 μm) (mag)	(4.5 μm) (mag)	P (days)	P [4.5] (days)	2nd Fit (days)	2nd[4.5] (days)	Amp. (mag)	Color (mag)	$\sigma_{[3.6]-[4.5]}$ (%)	Flag
DDO 216	45582	352.2400208	14.61585045	16.65	16.46	101	...	131	...	0.35	IE
DDO 216	58694	352.2214661	14.70353794	15.80	15.07	389	389	482	354	1.05	0.70	13.5	RF
DDO 216	76368	352.1983032	14.75455666	16.98	16.06	1308	196	223	178	0.34	0.92	16.2	IE
DDO 216	77533	352.1968384	14.73819065	17.04	15.91	103	174	110	1008	0.23	1.14	13.9	UF
DDO 216	83518	352.1894836	14.68728733	16.11	15.62	212	212	1339	1339	0.48	0.52	11.8	UF

Note. Column 2 lists the DUSTINGS IDs from Paper II, except for IDs over 5 million, which are new in this work. Columns 5 and 6 list the midline 3.6 and 4.5 μm magnitudes taken from the midline values of the best-fit light curve, columns 7 and 9 show the best- and second-best-fit pulsation periods (P , 2nd fit), columns 8 and 10 list the same values for the 4.5 μm fit, column 11 lists the fitted peak-to-peak 3.6 μm amplitude, columns 12 and 13 list the median and standard deviation of the [3.6]–[4.5] color, and column 14 lists a quality flag for a high-confidence reliable fit (RF), insufficient epochs (IE), an unreliable fit (UF), or an LPV 5000+ (see Section 5.4). The full catalog ($n = 261$) is available in the electronic version and on VizieR.

(This table is available in its entirety in machine-readable form.)

had at least three epochs with color values. We refer to these photometric points as “simulated” photometry and show them in our light curves as empty circles (Appendix A, Figure 9).¹⁵ We have similarly fitted the light curves of any sources with at least six epochs of 4.5 μm data using simulated 4.5 μm photometric values when possible. Only one source (IC 10 57276) did not have enough epochs to fulfill this requirement. These data are less sensitive (and therefore noisier), so we include them in Table 3 but use only the [3.6] data for further classification. For 65% of the full sample, the 3.6 and 4.5 μm periods are the same. For 87% of the sample, the periods agree to within 10%. For the remaining 11 sources, the standard deviation of the [3.6]–[4.5] color is large, and there is a difference in the number of epochs for all but two of the sources.

3.4. Light-curve Categorization

The light curves that pass the three criteria listed in the previous section are further categorized based on our confidence in the fits. These fall into four categories, two each considered “high-confidence” and “low-confidence.” These groups are discussed further in Sections 4.1 and 4.2; the phased and unphased light curves of the high-confidence variables are shown in Appendix A.

High-confidence variables are as follows.

1. Reliable-fit (RF) sources with light curves that pass a visual inspection, meant to isolate sources with unique fit solutions.
2. LPV 5000+ sources that do not necessarily have RFs but are clearly variable on long timescales; described further in Section 5.4.

Low-confidence variables are as follows.

1. Insufficient epoch (IE) variable sources with RFs but where the uniqueness of the fit is unclear.
2. Unreliable-fit (UF) variable sources that do not pass visual inspection.

Recall that both the high- and low-confidence variables have a χ^2 of at least 95% (Section 3.3), yet additional information about the uniqueness or quality of the fit is taken into account. The sources categorized as IEs are sources where a unique fit

solution to the unphased light curve is not visibly clear. This may include a light curve lacking temporal coverage toward the maximum or minimum of the light curve, or where a shorter pulsation period could plausibly fit the source. A source designated as a UF is typically one that has a change in brightness in several epochs that is in the opposite direction of the change in the best-fit unphased light curve, outside the value of the uncertainty. Figure 12 in Appendix B shows examples of IE and UF sources.

We show the average [3.6]–[4.5] versus absolute 3.6 μm magnitude color–magnitude diagram (CMD) of both high- and low-confidence sources in Figure 2. It is clear that we are only sensitive to the highly evolved and dusty x-AGB stars here, as relatively dust-free C-AGB and O-AGB stars have smaller amplitude pulsations closer to the level of our photometric uncertainty (Riebel et al. 2015). We are also less sensitive to shorter-period variables due to our observing cadence. As a result, we do not obtain any high-confidence variables with median [3.6]–[4.5] colors less than 0.1 mag, and most of our measured pulsation periods are longer than 200 days.

Our final results include 92 high-confidence variables with four LPV 5000+ and 88 RF sources with a median period of 437 days. Figure 3 shows the variability of our low- and high-confidence variables. Note that UF sources cluster toward a low-variability index. We categorize the LPV 5000+ sources as high-confidence variables, but with a limited temporal baseline, we cannot definitively confirm their periodicity. The light curves of the low- and high-confidence variables are available for download in the electronic version and on VizieR.

4. Results

4.1. High-confidence Variables

Figure 2 shows that the high-confidence variables occupy the same space as the x-AGB sources found in the SAGE program (Riebel et al. 2010). The RF sample has a median 3.6 μm absolute magnitude of $-9.2 \pm 0.26(1\sigma)$. Four high-confidence variables have IR colors much redder than the rest of the sample ([3.6]–[4.5] > 1): IC 10 98211, IC 10 105991, NGC 185 90369, and WLM 84699. Their light curves, as well as the rest of the RF sources, are shown in Figure 9. We were not able to detect any RFs in And IX, Sextans B, or Sag DIG. This is not surprising, given that And IX and Sag DIG have limited temporal coverage and a small AGB population.

¹⁵ The displayed errors for the simulated photometry include the $\sigma_{[3.6]-[4.5]}$ and 4.5 μm photometric uncertainties.

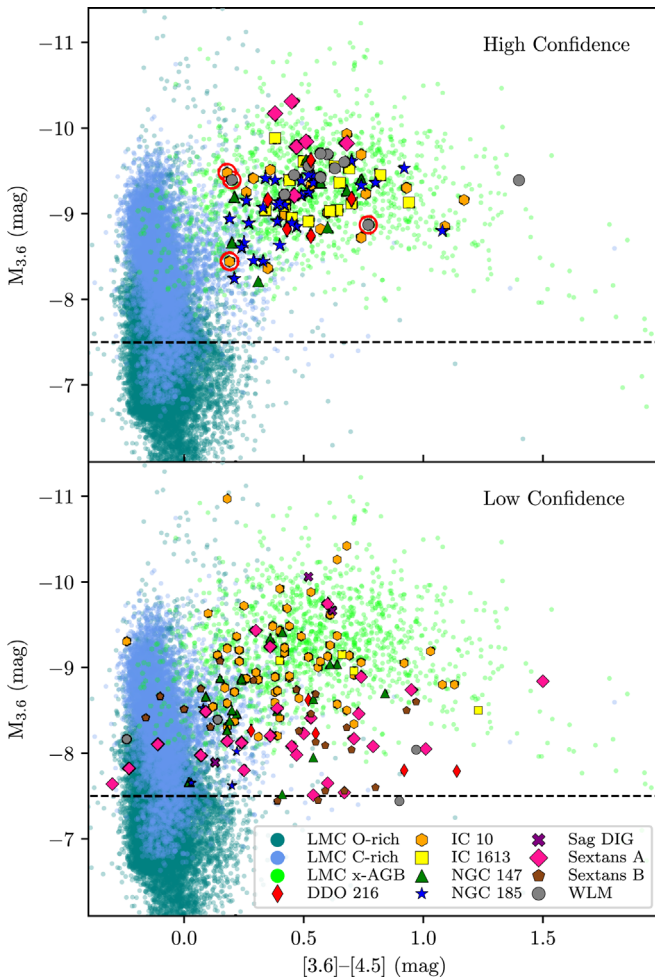


Figure 2. Average *Spitzer* IRAC [3.6]–[4.5] vs. $3.6\ \mu\text{m}$ absolute magnitude for the high- (top) and low-confidence (bottom) DUSTiNGS sources compared to the LMC sample from Riebel et al. (2010). Here $M_{3.6}$ was calculated using the midline value of the best-fit light curve. The brightness threshold for our light-curve fitting analysis is shown with the dotted line. The LPV5000+ sources (described in Section 3.3) are shown with red circles. Adopted distances to the DUSTiNGS galaxies are shown in Table 1. For the LMC, we adopt a distance modulus of $M - m = 18.52$ mag (Kovács 2000).

4.2. Low-confidence Variables

The low-confidence sample is composed of 113 sources with IEs and 56 sources with UFs. The low-confidence variables have a median absolute magnitude of $-8.55 \pm 0.17(1\sigma)$, which is low compared to most of the LMC x-AGB sample. Sextans B has 14 sources with IEs and 12 sources with UFs. This may be the result of stochastic sampling. At fainter magnitudes, the photometric uncertainty is higher, making it more difficult to detect changes in brightness. This likely indicates that some sources in the low-confidence sample are not LPVs but in fact YSOs and AGNs, which sometimes show irregular variability in the IR. We expect that low-confidence sources that cluster together may be YSOs in a star formation region. Sources far from the galaxy center may be AGNs. However, given the nonuniform positioning of the detectors and our sporadic temporal coverage, these sources are hard to disentangle (Paper I).

4.3. Detection Statistics

Of the sources that were included in our light-curve analysis, we have isolated a small subset as potential AGB stars from their

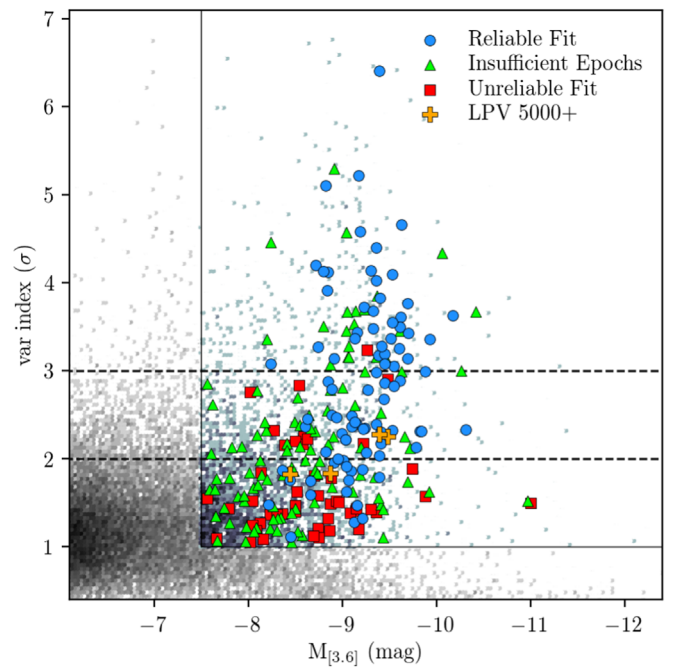


Figure 3. Standard deviation of the $3.6\ \mu\text{m}$ magnitude of the light curve divided by the average photometric uncertainty (variability index) vs. absolute $3.6\ \mu\text{m}$ magnitude for the DUSTiNGS sources with fitted light curves. Small points are those that did not meet the requirements of our light-curve fitting analysis (gray) and those that met the criteria but were not considered credible enough for further analysis (bluish). The 2σ and 3σ intervals are shown with dotted lines, and the designation of “LPV 5000+” is described further in Section 5.4.

Table 4
Results of Light-curve Fitting

Galaxy	Initial Sample	Var. Index > 2	Dusty and Variable	Low Conf.	High Conf.
And IX	16	2	1	0	0
DDO 216	24,688	2166	15	7	5
IC 10	80,351	5555	228	59	18
IC 1613	311	96	27	5	15
NGC 147	60,446	3712	70	20	8
NGC 185	53,011	3506	58	4	29
Sag DIG	51	10	8	3	0
Sextans A	22,946	2959	83	40	6
Sextans B	22,629	2281	89	26	0
WLM	33,184	2860	34	5	11
Total	308,083	24,160	613	169	92

Note. The table lists the number of high- and low-confidence variables per galaxy. Also shown is the number of sources and the number of sources that we determined were variable (variability index > 2) and dusty and variable with $[3.6]-[4.5] > 0.2$ mag and a variation in the color of less than 20%.

$[3.6]-[4.5]$ color and variability alone. These sources have already been limited to those that have at least six epochs and are bright in the IR ($M_{[3.6]} < -7.5$ mag). Table 4 shows the number of variable sources (var. index > 2) in this sample and the number of sources that were dusty ($[3.6]-[4.5] > 0.2$) and also variable. Many of the sources that we were not able to confirm as AGB stars may be less luminous and dusty. These may have been confirmed as AGB stars given more observations.

In Paper II, we showed that our photometry is sensitive enough to detect variability down to peak-to-peak amplitudes of ~ 0.15 mag. We have now compared the number of sources with

Table 5
Comparison to Literature Periods

Galaxy	ID	ID _{Lit.}	R.A. (deg)	Decl. (deg)	P (days)	$P_{\text{Lit.}}$ (days)	Type	Flag
IC 1613	95038	1093	16.24090	2.15469	318	305	C	RF
IC 1613	142830	3198	16.18219	2.05673	395	370	C	RF
NGC 147	68407	112	8.35656	48.55440	449	406	...	RF
NGC 147	112918	171	8.27302	48.47706	385	...	C	RF
NGC 147	113288	158	8.27241	48.50505	317	226	C	IE
NGC 147	123715	161	8.25264	48.46111	335	371	...	UF
NGC 185	70862	009	9.79879	48.32867	196	277	C	RF
NGC 185	77053	313	9.78671	48.35519	418	519	...	RF
NGC 185	83286	049	9.77481	48.38233	416	399	M	RF
NGC 185	87065	062	9.76783	48.36058	226	219	...	RF
NGC 185	87213	398	9.76754	48.35008	837	427	...	RF
NGC 185	89650	384	9.76315	48.32895	637	82	S	RF
NGC 185	91361	076	9.76007	48.31672	360	358	C	RF
NGC 185	92015	078	9.75888	48.32191	416	420	S	RF
NGC 185	95982	404	9.75180	48.32625	381	367	...	RF
NGC 185	96014	099	9.75173	48.32416	327	287	C	RF
NGC 185	131142	249	9.68842	48.33260	227	231	...	RF
NGC 185	136723	160	9.67694	48.31031	347	361	C	RF
NGC 185	132331	396	9.68612	48.35306	227	234	C	UF

Note. Literature values (Lit.) are from Menzies et al. (2015) and Lorenz et al. (2011), where pulsation periods were derived using near-IR photometry (*JHK*).

high-confidence RFs that were covered in each epoch of the Cycle 11 observations with the number of 3σ x-AGB stars from Paper II also found in that region (Appendix C). Of the 3σ variables originally detected in Paper II and categorized as x-AGB stars, we have confirmed 19% as RFs and likely TP-AGB stars. The remaining Paper II variables are outside of our spatial footprints and/or have temporal coverage that is too sporadic to measure a reliable light curve. The variable star catalogs presented here should therefore be considered a representative subset of the total variable population in each galaxy.

Previously, LPVs have been detected in four of our galaxies: IC 1613 (Menzies et al. 2015), NGC 147, NGC 185 (Lorenz et al. 2011), and Sag DIG (Whitelock et al. 2018). We have classified 19 of these previously detected sources as high-confidence LPVs. The pulsation periods measured in these works are comparable to those measured in this work (Table 5).

5. Discussion

Our new sample of LPVs allows us to study the pulsation properties of evolved stars in metal-poor environments and how they are affected by other observable parameters. These results along, with previous observations, suggest that dust production is unaffected by metallicity.

5.1. Dust and Pulsation

The [3.6]–[4.5] color has been shown to scale approximately with the dust content (Paper II; Riebel et al. 2015). Within our sample, both pulsation period and (especially) pulsation amplitude also correlate well with [3.6]–[4.5] color¹⁶ (Figure 4). This correlation has been seen in more metal-rich samples in the galaxy, Magellanic Clouds, M33, and Sgr dSph (Whitelock et al. 2006; McQuinn et al. 2007; Javadi et al. 2011a; McDonald et al. 2014; Riebel et al. 2015). We see in Figure 5 that our amplitudes are unaffected by changes in

metallicity. Based on these relationships, it follows that dust production should also be unaffected by metallicity.

Uncertainties—There are uncertainties underlying our assumptions of dust production and metallicity. Given that most of our LPVs are expected to be carbon stars, we can only claim that dust production is unaffected by metallicity for carbon stars. The [3.6]–[4.5] color, a key metric in this analysis, will also depend on the dust temperature and wind speed, and the opacity of the dust may also differ at lower metallicities (McDonald et al. 2011, 2019). In determining the impact of metallicity on the dust production, we have assumed metallicities for our sample that were derived primarily from samples of RGB stars. These stars represent populations older and more metal-poor than our intermediate-mass LPVs. We expect the true metallicities of our LPVs to lie between these metallicities and ISM gas-phase oxygen abundances (shown in Table 1), yet neither show a correlation with amplitude.

5.2. IR P – L Relation

Wood (2015) reviewed what is known about the P – L sequences of variable stars and suggested an evolutionary scenario with the current mass decreasing toward a longer period at a given luminosity. This allows us to follow the amount of mass that has been lost as a star moves toward the latest stages of its evolution.

Figure 6 shows period with respect to luminosity for our LPVs, with [3.6]–[4.5] color and metallicity in color. Our sample spans $\gtrsim 1$ dex in metallicity, providing a first look at how the IR P – L relation behaves at very low metallicity. Compared to the SAGE+MACHO sample (Riebel et al. 2010), most of our LPVs follow the fundamental-mode sequence. We find that the reddest objects fall below the fundamental mode at $3.6 \mu\text{m}$, a phenomenon that has also been seen in LPVs in the Magellanic Clouds (Ita et al. 2004b; Ita & Matsunaga 2011) and IC 1613 (Whitelock et al. 2017). These sources, likely obscured by circumstellar extinction, have a decreased $3.6 \mu\text{m}$ flux. In particular, IC 10 has a high number of reddened

¹⁶ Pulsation amplitude and period have also been seen to scale with mass-loss rate (Javadi et al. 2013; Goldman et al. 2017).

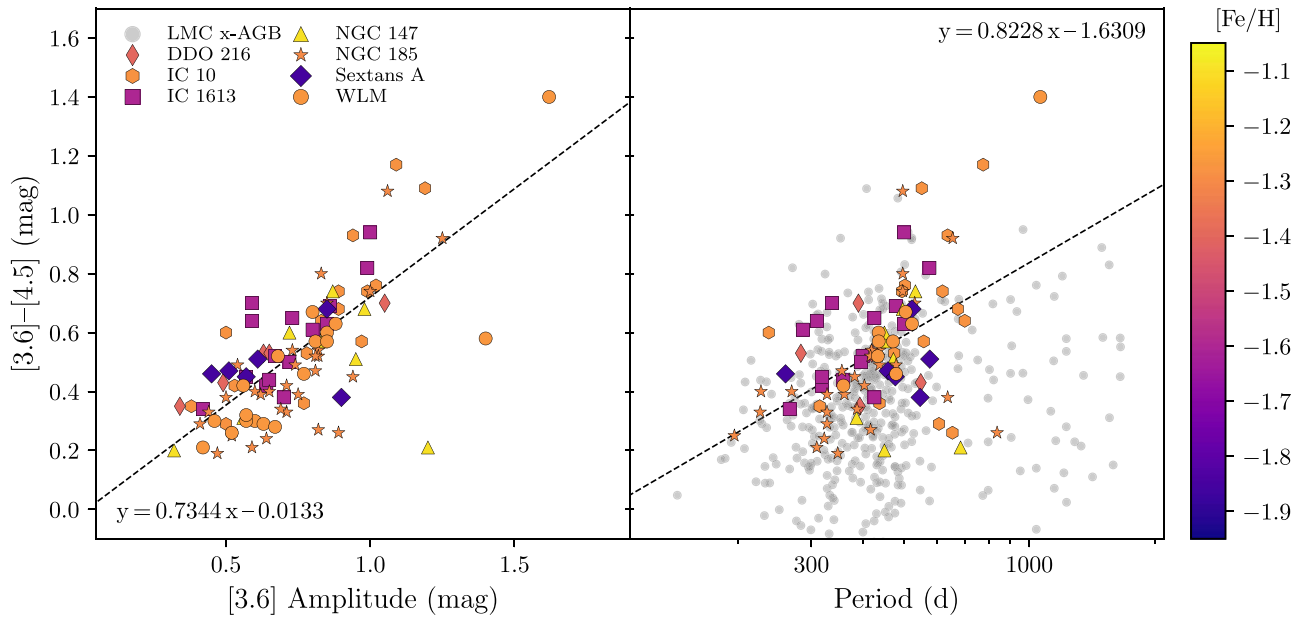


Figure 4. Pulsation amplitude and period of our RF sources vs. their *Spitzer* [3.6]–[4.5] color (indicative of dust content), with metallicity shown in color. The best-fit results and lines are shown in the figure. Also shown are pulsation periods for the x-AGB sample from the LMC (Riebel et al. 2010); 3.6 μm amplitudes were not measured. The low-confidence variables are shown in Figure 11. The cadence and number of epochs in the SAGE-Var survey (Riebel et al. 2015) are insufficient for getting reliable amplitudes, which may contribute to the scatter for the LMC sample.

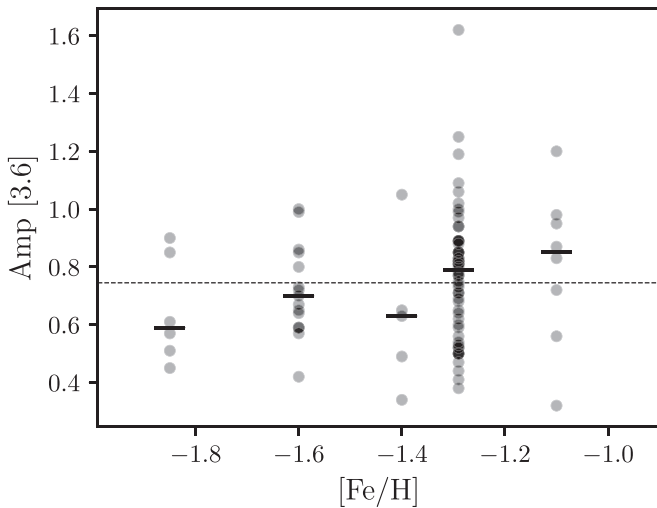


Figure 5. The 3.6 μm best-fit amplitudes with respect to [Fe/H]. The dotted line shows the median amplitude of the reliable-fit sample. Black lines show the median amplitude in five metallicity bins. There is an apparent increase of the median amplitudes towards higher metallicity. However, this trend is dominated by stochastic sampling.

sources, which may be a combination of circumstellar and, to a lesser degree, interstellar extinction. It lies near the Galactic plane and has an estimated interstellar extinction of $A_V \sim 2.33$ mag, which has been measured using a CMD analysis (Weisz et al. 2014). This should cause a mean approximate shift of ~ 0.2 mag in the IRAC magnitudes for which we have corrected for all sources in IC 10.

Our data suggest that, down to an [Fe/H] = -1.85 , the P – L relation of the fundamental mode (at 3.6 μm) is largely unaffected by metallicity. This suggests that the fundamental mode may be a robust tool for measuring distances to galaxies in the IR (e.g., Yuan et al. 2018). Since dusty AGB stars are among the brightest IR sources in galaxies, this technique can

reach more distant galaxies than what can currently be measured with tip of the red giant branch (TRGB) distance estimates. However, there is an ~ 1 mag uncertainty in the absolute magnitude stemming from the width of the fundamental-mode sequence at 3.6 μm . The spread of the sequence may be a result of differences in the current mass as a result of mass loss. For the DUSTINGS RF sources and x-AGB stars in the LMC that are firmly on the fundamental mode, we calculate the standard errors of the best fit of the x-AGB sample of 0.066 and 0.022, respectively. This excludes several shorter-period and fainter LPVs and several strongly affected by the circumstellar dust. The smaller standard error we calculate for the LMC sample is expected, given the galaxy’s larger and more complete sample and more accurately known interstellar extinction and distance. We modeled the LMC x-AGB P – L relation with three parameters: slope, intercept, and intrinsic scatter. We used a first-order Student t likelihood function, which has more weight in the tails than a Gaussian and is therefore less vulnerable to the effects of outliers (Galliano 2018). We sampled this likelihood function using PYMC3, a Monte Carlo Markov chain package for Python (Salvatier et al. 2016), with 5000 steps along 15 independent chains. Equation (1) shows the fit of the fundamental-mode x-AGB sample, calculated with a scatter of 0.25 ± 0.01 ; the fit is also shown in Figure 6:

$$M_{3.6} = -5.26_{-0.14}^{+0.15} \log P + 4.42_{-0.38}^{+0.38}. \quad (1)$$

Using the intercept error, this translates to a 4% uncertainty on the distance to a galaxy measured using the LMC P – L relationship. This is smaller than the $\sim 8\%$ uncertainty typically measured using the TRGB method (e.g., McQuinn et al. 2013) but uses only sources firmly on the fundamental mode. This may provide a more accurate tool at larger distances.

Using a similar approach as in Equation (1), we have also fitted the same LMC x-AGB sample at 4.5 μm with a scatter of

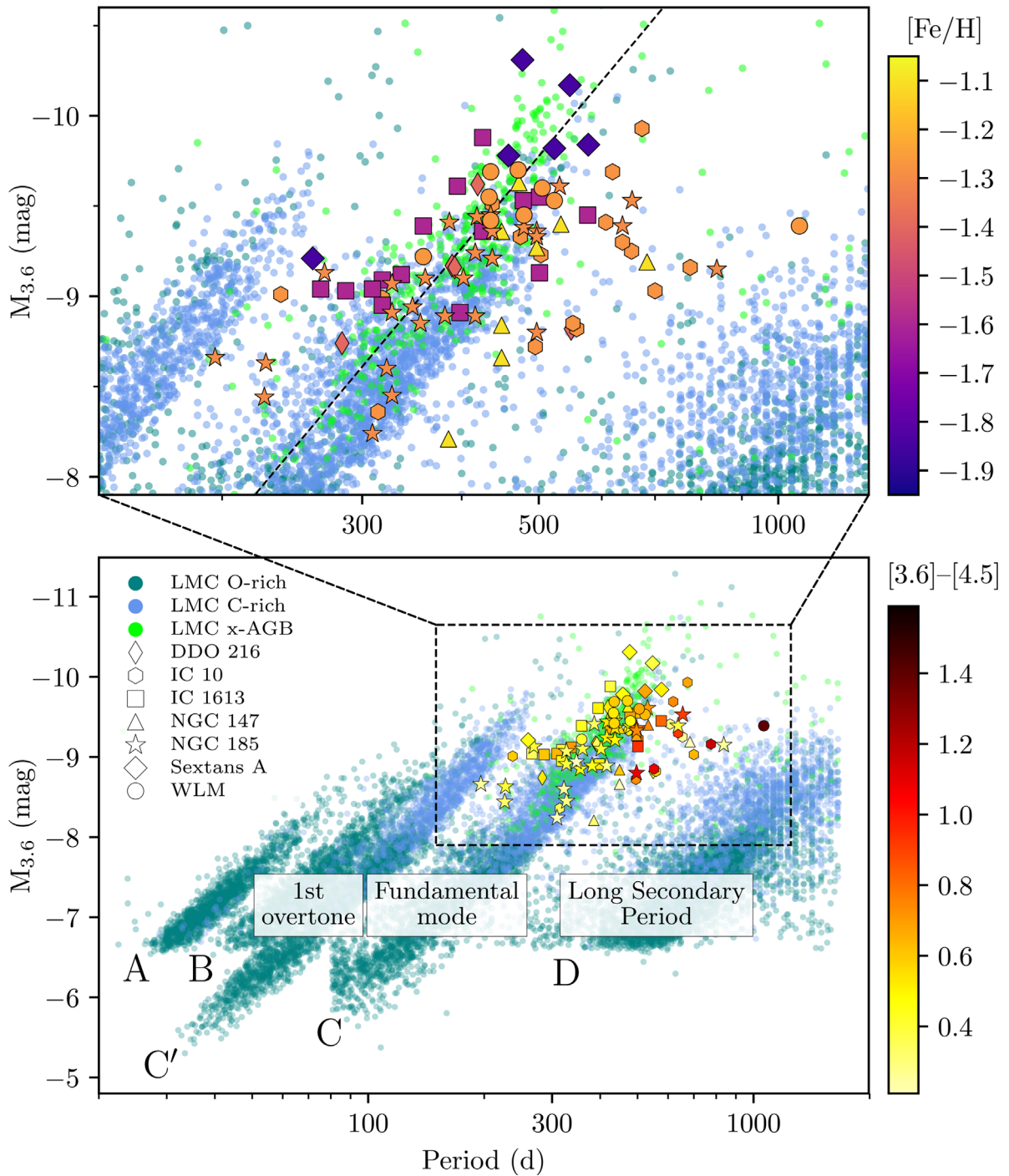


Figure 6. The P - L relation of the high-confidence DUSTiNGS sample, with the color of the symbols showing the metallicity (top) and $[3.6]-[4.5]$ color (bottom), as well as galaxy membership, indicated by shapes. We show the MACHO+SAGE sample from Riebel et al. (2010) containing oxygen- and carbon-rich AGB stars, as well as more evolved and dusty x-AGB stars of both spectral types from the DUSTiNGS and MACHO+SAGE samples. Also shown is the best fit of the LMC x-AGB sources that are clearly fundamental-mode pulsators. Here $M_{3.6}$ was calculated using the midline value of the best-fit light curve for the DUSTiNGS sample.

0.35 ± 0.01 :

$$M_{4.5} = -5.79^{+0.20}_{-0.21} \log P + 5.44^{+0.54}_{-0.53}. \quad (2)$$

At $4.5 \mu\text{m}$ (Figure 7), the RF LPVs appear to be associated with a shifted fundamental-mode sequence significantly affected by circumstellar dust. This dust will veil molecular features like CO, known to affect the P - L relation in Cepheids (Scowcroft et al. 2011; Blum et al. 2014). This shift off of the fundamental mode suggests that it may be more challenging to

use this wavelength region for measuring distance using the brightest and dustiest stars.

5.3. Classification of Stellar Chemistry with the HST

Some of our RF LPV sources were previously observed with the *Hubble Space Telescope* (HST; Paper IV); Figure 15 in Appendix C shows the footprints of these observations. Medium-band optical photometry in the F127M, F139M, and

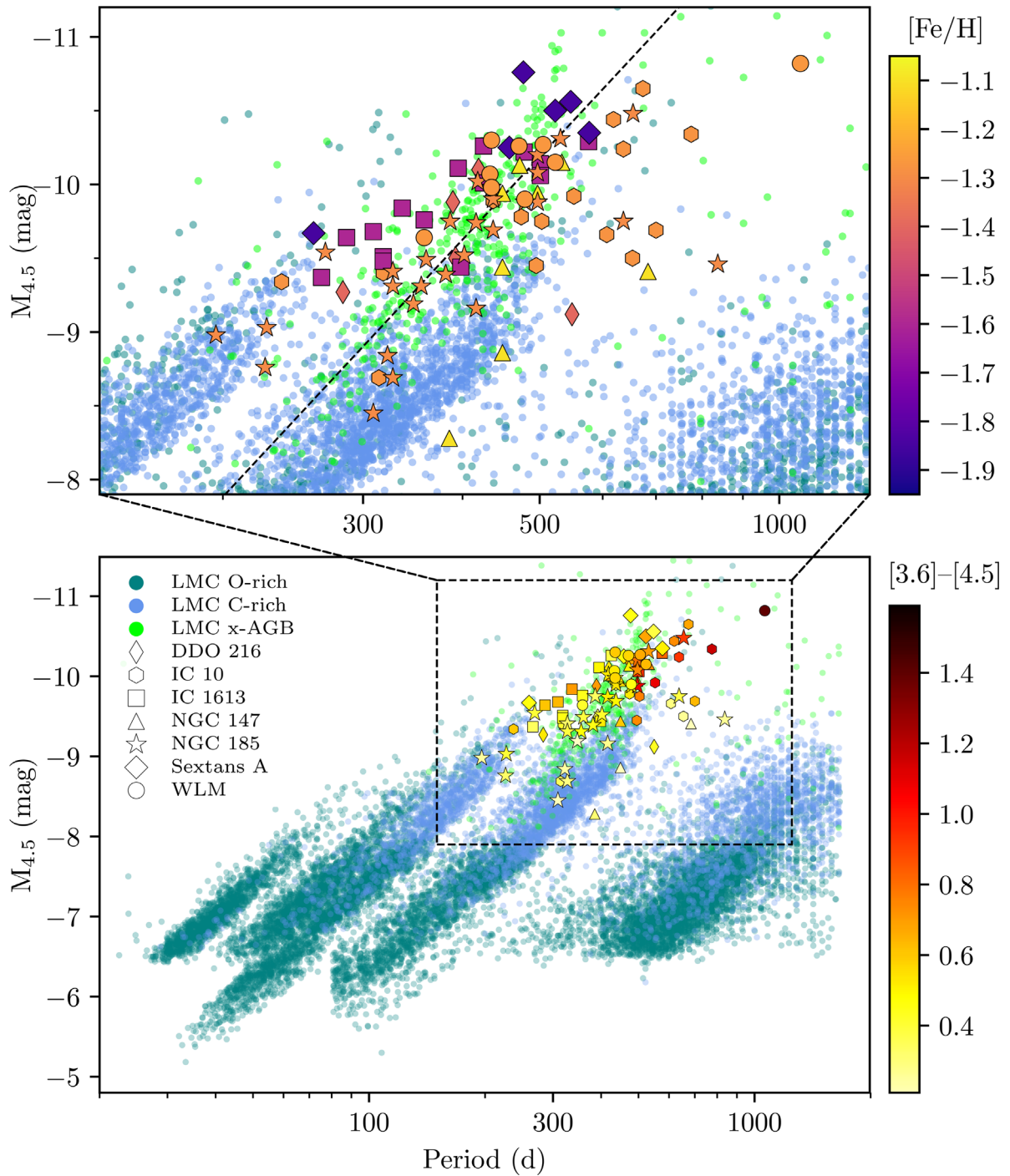


Figure 7. Same as Figure 6, but showing $4.5 \mu\text{m}$ magnitudes. Dusty stars get brighter at $4.5 \mu\text{m}$, creating a sequence more in line with the other sources. We see a tighter sequence than the sequence at $3.6 \mu\text{m}$, which is affected by the $[3.6]-[4.5]$ color.

F153M bands was used to categorize evolved stars by their chemical type (Paper IV). For our sample of RF LPVs, eight have *HST* counterparts with chemical types, all of which were found to be carbon-rich (Table 6). We found counterparts for nine sources with IEs, which include two oxygen-rich sources and seven carbon-rich sources with UFs. Theoretical models predict that most of these AGB populations will be dominated by carbon stars (Paper IV), with many fewer higher-mass oxygen-rich sources as a result of their metal-poor environments (Dell’Agli et al. 2016, 2018, 2019) and star formation histories (Hamedani Golshan et al. 2017; Javadi et al. 2017;

Goldman et al. 2018; Hashemi et al. 2019). Additionally, they may be too obscured in the near-IR, lack sufficient temporal coverage, or not covered in the *HST* observations. The fact that oxygen-rich LPVs have not been detected here is not proof that they do not exist.

5.4. Individual Sources

We have discovered several sources with particularly interesting light curves (Figure 8). And IX is the most metal-poor galaxy in our sample, and we detected one LPV candidate, And IX 5000004, that has a clear variability and is one of the

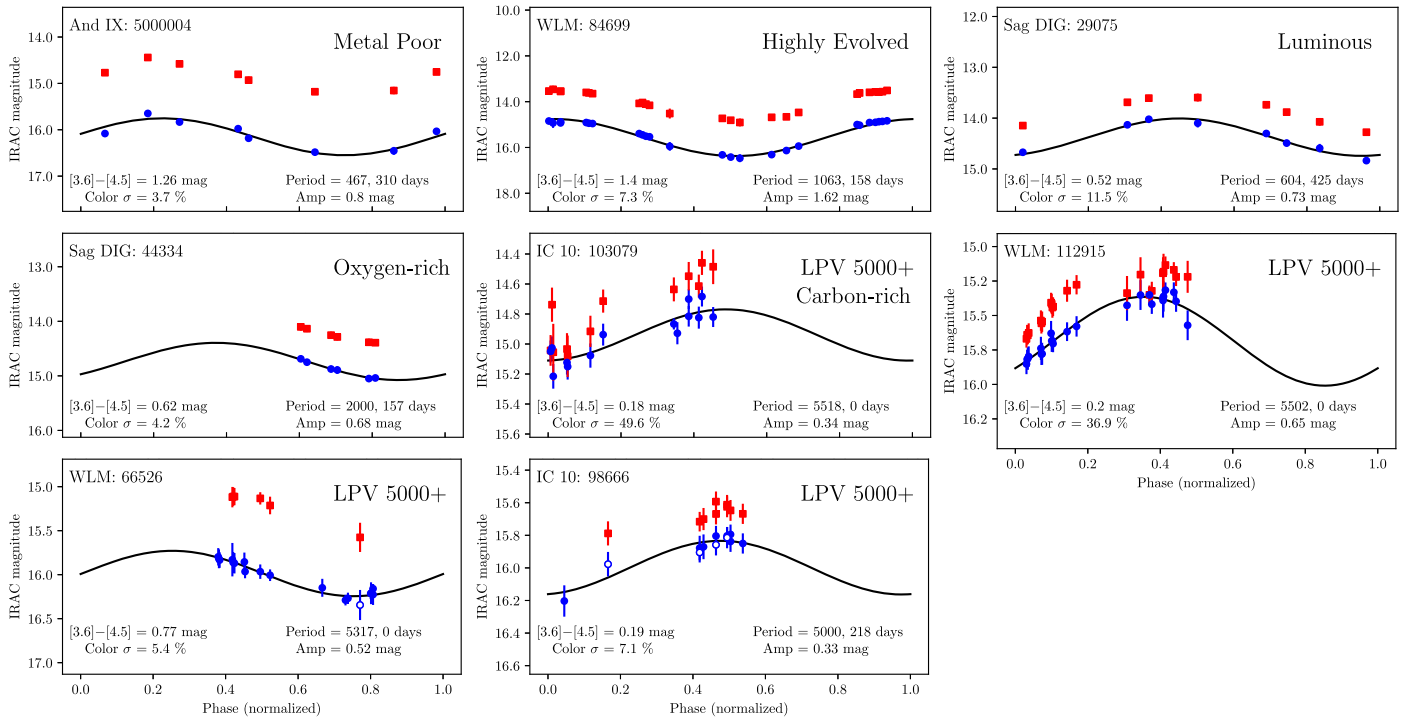


Figure 8. Light curves of particularly interesting sources with the IRAC 3.6 μm (blue) and 4.5 μm (red) photometry. Unless indicated, the error bars are smaller than the plotting symbols. Shown from top left to bottom right are examples of sources that are metal-poor, highly evolved and dusty, bright in the IR, categorized as oxygen-rich, and the four LPV 5000+ sources. The LPV 5000+ source IC 10 103079 also has a confirmed carbon-rich chemistry.

Table 6
DUSTiNGS Sources with Both Derived Pulsation Periods and Determined Chemical Type

(1)	(2)	(3)	(4)	(5)	(6)	(7)	(8)	(9)	(10)	(11)	(12)	(13)
Galaxy	ID	R.A.	Decl.	Type	Period (days)	[3.6] amp (mag)	F127M (mag)	F139M (mag)	F153M (mag)	[3.6] (mag)	[4.5] (mag)	Flag
NGC 147	68407	00:33:25.61	+48:33:15.1	C	449	0.83	20.18	19.71	19.35	14.98	14.43	RF
NGC 147	112918	00:33:05.55	+48:28:37.2	C	385	0.54	19.45	19.09	18.80	16.24	15.94	RF
DDO 216	96974	23:28:41.54	+14:44:45.9	C	392	0.34	19.76	19.24	18.94	15.70	15.35	RF
DDO 216	98916	23:28:40.97	+14:44:01.3	C	283	0.63	20.36	19.90	19.48	16.08	15.55	RF
DDO 216	101247	23:28:40.29	+14:44:38.1	C	419	0.65	19.26	18.80	18.33	15.29	14.76	RF
Sextans A	86434	10:11:00.77	-04:41:54.0	C	458	0.51	20.18	19.71	19.54	16.01	15.54	RF
Sextans A	90941	10:10:59.20	-04:42:23.0	C	260	0.45	20.27	19.82	19.67	16.53	16.07	RF
Sextans A	98908	10:10:56.45	-04:41:33.0	C	477	0.57	20.27	19.79	19.41	15.57	15.12	RF
IC 10	101088	00:20:15.71	+59:16:00.9	C	215 ^a	0.56	19.99	19.47	19.19	15.70	15.33	IE
IC 10	101812	00:20:15.24	+59:15:59.3	C	210 ^a	0.41	18.90	18.33	18.08	14.89	14.68	IE
IC 10	109003	00:20:10.26	+59:20:10.4	C	170 ^a	0.32	18.07	17.65	17.46	14.65	14.27	IE
IC 10	109003	00:20:10.17	+59:20:11.6	M	170 ^a	0.32	19.54	19.24	18.80	14.65	14.27	IE
IC 10	111369	00:20:08.84	+59:16:57.6	C	170 ^a	0.69	19.22	18.70	18.47	15.58	15.03	IE
IC 10	117441	00:20:04.56	+59:21:11.8	C	132 ^a	0.44	18.54	18.15	17.98	15.92	15.74	IE
NGC 147	55735	00:33:32.28	+48:32:47.3	C	133 ^a	0.31	18.69	18.34	18.20	15.92	15.70	IE
NGC 147	113288	00:33:05.40	+48:30:18.1	C	317 ^a	0.49	18.08	17.69	17.55	15.83	15.63	IE
Sag DIG	44334	19:29:57.95	-17:40:17.0	M	2000 ^a	0.68	18.03	17.72	17.26	14.88	14.26	IE
IC 10	65446	00:20:39.81	+59:16:39.2	C	854 ^a	0.35	19.52	19.04	18.73	15.79	15.53	UF
IC 10	65548	00:20:39.74	+59:17:25.3	C	136 ^a	0.43	19.84	19.37	19.03	15.73	15.33	UF
IC 10	73607	00:20:34.08	+59:15:58.1	C	695 ^a	0.41	19.40	18.89	18.53	15.32	15.10	UF
IC 10	107394	00:20:11.34	+59:21:14.5	C	555 ^a	0.80	20.14	19.64	19.39	16.01	15.58	UF
IC 10	114178	00:20:06.78	+59:19:57.2	C	378 ^a	0.40	19.46	18.99	18.66	15.70	15.37	UF
Sextans A	91449	10:10:59.05	-04:40:14.0	C	524 ^a	0.36	20.61	20.07	19.77	16.07	15.47	UF
IC 10	103079	00:20:14.25	+59:19:07.0	C	18.93	18.41	18.20	15.14	14.98	LPV 5000+

Note. The DUSTiNGS LPVs with *HST* photometry used to determine the spectral type (Paper IV). Columns 11 and 12 show the average magnitudes of all of the 3.6 and 4.5 μm epochs. Flag is the same as in Table 3.

^a Value unlikely due to the low confidence of the fit solution.

reddest sources in our sample. It lies near the outer regions of M31's disk at 37 kpc from the galaxy's center and, while unlikely, could be a metal-rich M31 interloper. More epochs are needed to constrain the precise period, and spectroscopy is needed to confirm its membership in And IX.

Our most massive source is WLM 84699, with a pulsation period of 1063 days, fitted peak-to-peak pulsation amplitude of 1.62 mag at $3.6 \mu\text{m}$, and $[3.6]-[4.5]$ color of 1.6 mag. This is indicative of a very late stage of evolution, a high mass-loss rate, and a high dust production rate. This source was also analyzed in Karambelkar et al. (2019) and lies between the lower-mass population of Mira variables and what they claim are massive AGB stars in the $P-L$ diagram. These massive AGB stars are also in galaxies with younger populations than WLM, making it a particularly interesting target for spectroscopic follow-up and an analysis of the source's dust composition.

While not as evolved, Sag DIG 29075 is our most luminous source and also quite metal-poor, but more observations are needed to constrain the period. Another source within Sag DIG, 44334, was previously categorized in Paper IV as oxygen-rich, making it one of the most metal-poor and dusty oxygen-rich evolved stars known. This source has a known pulsation period of 950 days from ground-based observations in the near-IR (Whitlock et al. 2018). We lack enough IR data to further constrain the period. However, the clear variable nature of the source, together with its red color, strongly suggest that it is producing dust.

The remaining four sources in Figure 8 have been categorized as LPV 5000+ and show a gradual change over the entirety of the light curve. While these sources may be shorter-period evolved stars with a coincidental cadence, they may also have dominant pulsation periods that are considerably longer than a typical AGB star ($P \gtrsim 2000$ days) or may just be growing or diminishing in brightness with no periodicity. Only one of the LPV 5000+ sources (IC 10 103079) has been confirmed as carbon-rich and thus an AGB star (Paper IV).

5.5. Long Secondary Period

Distinct from the LPV 5000+ are sources with LSPs. The sequence hosts less-evolved stars, as well as TP-AGB stars, with periods between 400 and 1200 days. Recent work by Wood (2015) and Trabucchi et al. (2017, 2018) has improved our understanding of how stars evolve along these sequences, but the mechanism that drives the LSP is still unclear. It is now known that stars with primary periods associated with the LSP, sequence D, have secondary periods that lie in the middle of the first-overtone sequence made up of B and C'. The reason for the appearance of the sequence-D period in these stars is unknown but may arise from convection, binarity, or changes in the internal chemistry of the star (Nicholls et al. 2009; Mathias et al. 2018). The pulsation behavior of our LPV 5000+ sources may be that of an LSP.

5.6. High-redshift Dust

Our observations provide further evidence of the evolved nature of the dusty sources found in metal-poor galaxies and for significant AGB dust production in these environments. The lowest metallicities of our LPV sample are characteristic of galaxies ~ 12.3 Gyr ago and redshifts of $z \sim 5$ (Rafelski et al. 2012; Poudel et al. 2017). Paper IV identified both carbon- and

oxygen-rich evolved stars at low metallicity. As luminous oxygen-rich sources are more massive than their lower-mass carbon-rich counterparts, they are capable of injecting dust into the ISM as early as 30 Myr after forming (for a $10 M_{\odot}$ star), while carbon stars are expected to take longer (as soon as $\sim 200-300$ Myr; Sloan et al. 2009). Most dust evolution models ignore dust produced by metal-poor oxygen-rich stars.

While we expect that AGB stars may produce dust in this regime, it is unclear whether they are the dominant dust producers. Supernovae may produce considerable dust; however, their net contribution is still unclear due to the unknown efficiency of dust destruction (Lakićević et al. 2015; Temim et al. 2015). Another alternative is dust produced by grain growth within the ISM (Zhukovska et al. 2008). However, a theory as to how the grains grow and what seeds their nucleation has yet to be identified. While the pulsation properties and $3-5 \mu\text{m}$ observations highlight the important role that AGB stars play in dust production, longer-wavelength observations are critical to constraining the amount of cooler dust surrounding these stars. More observations are needed to confirm that AGB stars are capable of producing dust out to $z \sim 6$. The soon-to-launch *James Webb Space Telescope* (*JWST*) will allow us to study Local Group AGB samples in much greater detail. In particular, observations with the *JWST* Mid-infrared Instrument (Rieke et al. 2015) will be able to obtain photometry for every star in this sample out to $25 \mu\text{m}$ (Jones et al. 2017).

6. Conclusion

This survey has provided the first IR light curves of dusty evolved stars in metal-poor environments. We surveyed 10 metal-poor dwarf galaxies within 1.5 Mpc at 3.6 and $4.5 \mu\text{m}$. By combining our multi-epoch observations with archival observations, we identified the dustiest evolved AGB stars within these galaxies, sources that may have been missed in the near-IR or optical surveys due to dust obscuration. We have identified 88 sources in seven of these galaxies as high-confidence LPV candidates, eight of which have been confirmed as carbon-rich.

We find that metallicity does not seem to have a strong impact on AGB pulsation or dust production. This has implications for the dust seen at high redshift and the origin of dust in the early universe. We also find that the fundamental mode of the IR $P-L$ relationship seems unaffected by metallicity, at least between one-half and one-hundredth solar. This suggests that the $P-L$ relation can be a useful tool in measuring distance. With IR observations with *JWST*, the $P-L$ relation can be used to confirm distances to Type Ia supernovae in distant galaxies, providing additional constraints on the Hubble constant (H_0).

We would like to thank the SPIRITS team (PI: Mansi Kasliwal) for assistance with the inclusion of the SPIRITS data in four of our galaxies and Chris Clark for his help with the $P-L$ distance uncertainty calculation. This work is supported by *Spitzer* via grant GO11041 and the NASA Astrophysics Data Analysis Program grant No. NNX16AT56G. R.D.G. was supported by NASA and the United States Air Force. O.C.J. has received funding from the European Union's Horizon 2020 research and innovation program under Marie Skłodowska-Curie grant agreement No. 665593 awarded to the Science and Technology Facilities Council.

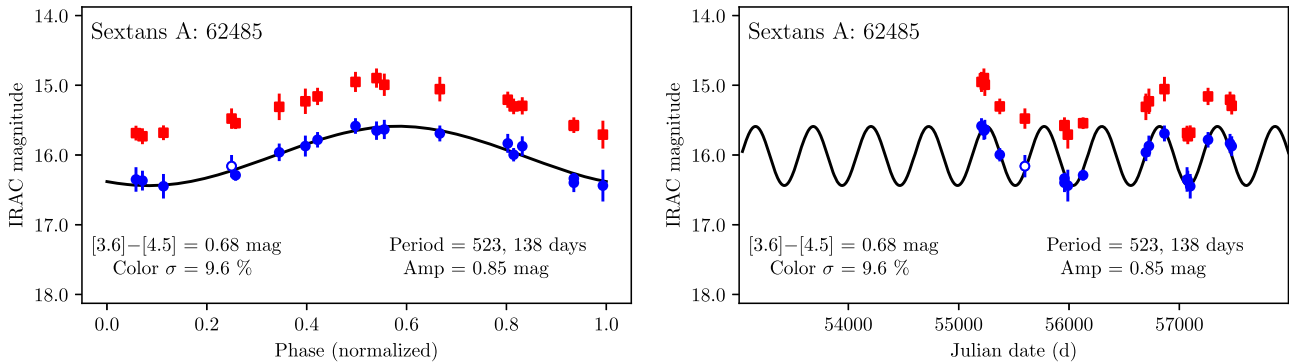


Figure 9. Our sample of high-confidence fit light curves. Shown are the IRAC 3.6 μm (blue) and 4.5 μm (red) photometry and the best-fitting periodogram fitted to the [3.6] data. Unless otherwise indicated, the data error bars are smaller than the plotting symbols. Also shown is our “simulated” photometry, denoted using open circles (see Section 3.2). The two numbers listed as period are the best- and second-best-fit values. Also shown is the best-fit 3.6 μm amplitude. Sextans A (62485) is given as an example, with the phased light curve on the left and the unphased light curve on the right. The complete figure set (88 images) is available in the online journal.

(The complete figure set (88 images) is available.)

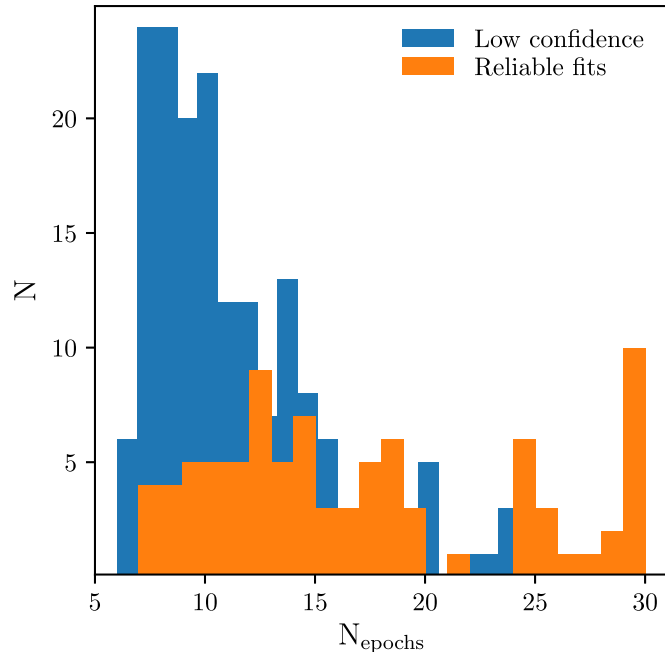


Figure 10. Histogram of the number of epochs for the RF and low-confidence LPVs. Light curves with less than 10 epochs are typically categorized as low-confidence LPVs.

Appendix A IR Light Curves

This appendix shows the phased and unphased light curves of the RF LPVs (Figure 9). The IRAC 3.6 μm (blue circles) light curves were fit with simple single-term sinusoidal functions using the Lomb–Scargle algorithm. Also shown are the corresponding 4.5 μm magnitudes (red squares). Simulated 3.6 μm photometry (see Section 3.2) are shown as open circles. Figure 10 shows the number of epochs for our RF and low-confidence LPVs.

Appendix B Low-confidence DUSTINGS Variables

From our visual examination of our sources, we have categorized them into two groups: high- and low-confidence LPVs (described in 3.3). The low-confidence variables are those with IEs to constrain the light curve or a poor fit of the model to the data. For the low-confidence variables, we show the P – L relation and how the pulsation behavior is affected by the [3.6]–[4.5] color in Figures 11, 13, and 14. Examples of low-confidence light curves are shown in Figure 12; high-confidence variables are shown in Figure 6.

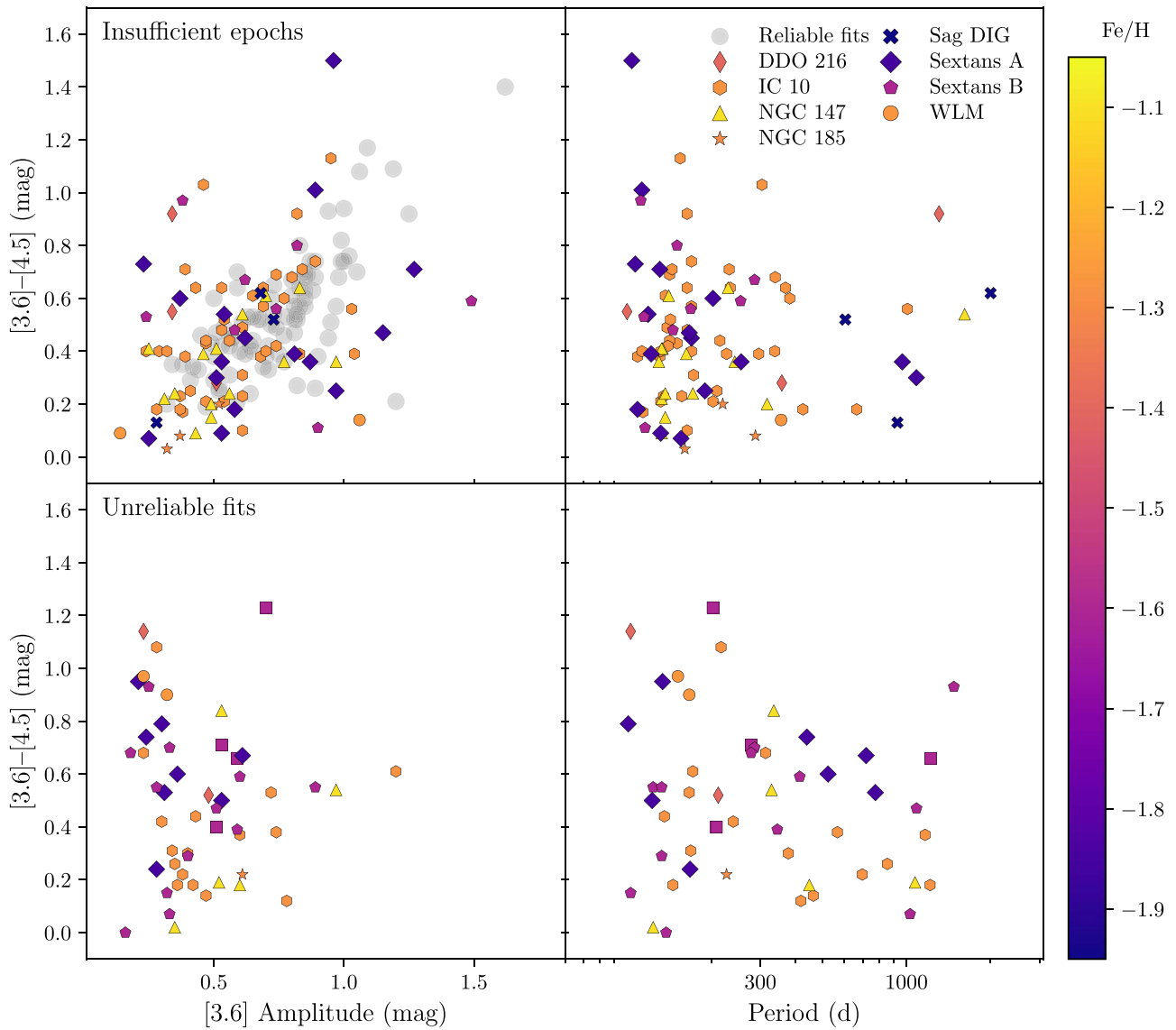


Figure 11. Same as Figure 4, but showing the sources designated as IE (top) and UF (bottom). While accurate periods could not be measured, the amplitudes are expected to be more accurate.

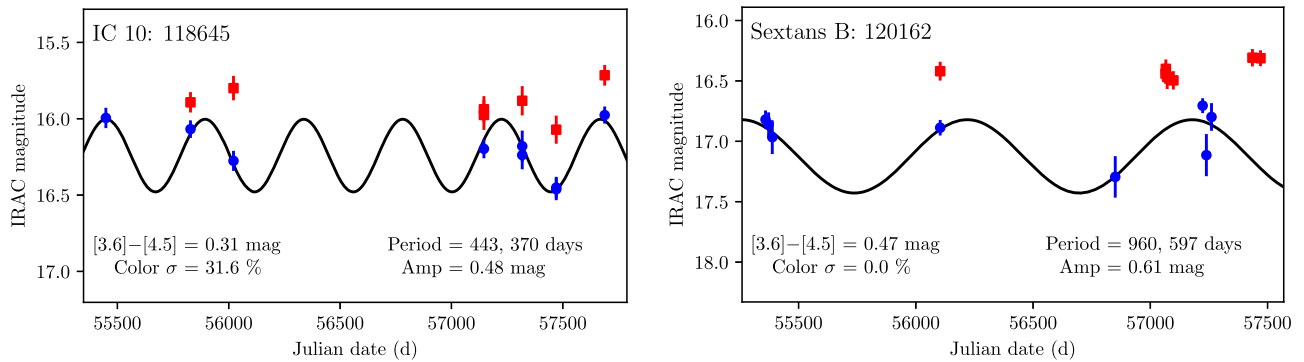


Figure 12. Examples of light curves with IEs (left) and a UF (right). The classification of IEs is only made if an RF source could plausibly be fit with a shorter or longer period.

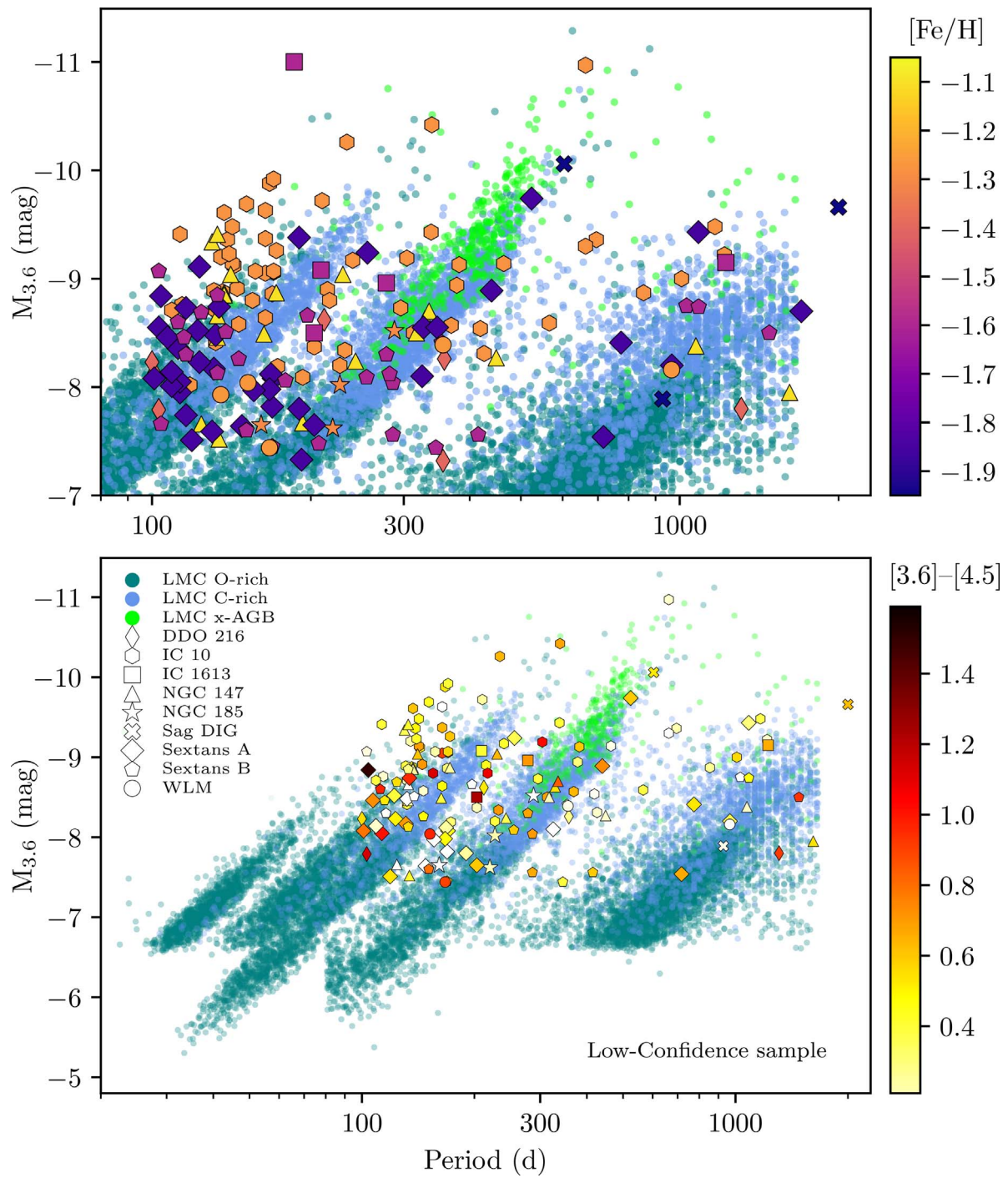


Figure 13. Same as Figure 6, but showing the low-confidence variables.

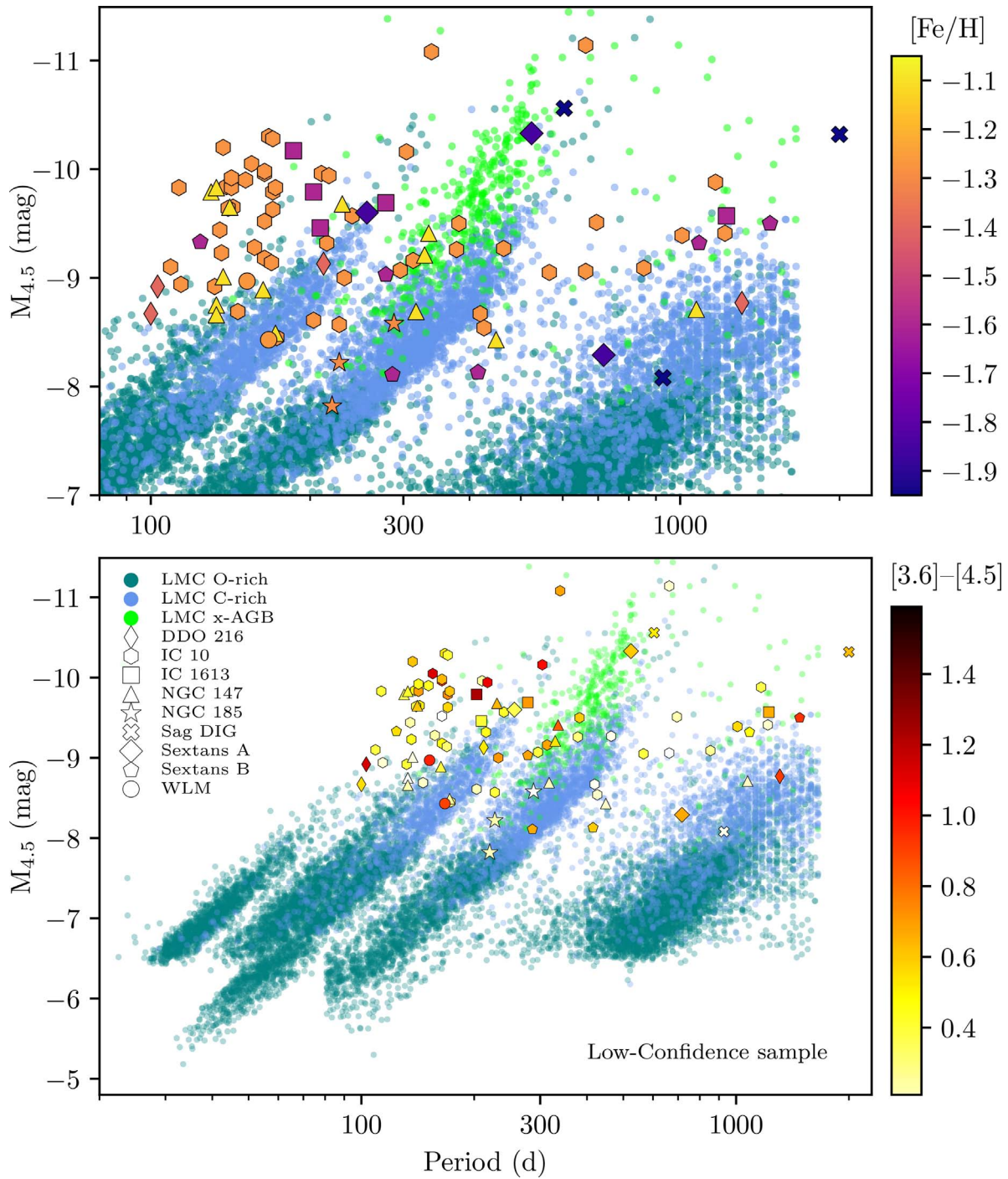


Figure 14. Same as Figure 13, but showing the 4.5 μm magnitudes.

Appendix C DUSTiNGS Spatial Distribution

We have mapped the spatial distribution of the high- and low-confidence DUSTiNGS LPVs on the *Spitzer* mosaics from Paper I (Figure 15). Also shown are the footprints of the *HST* observations used in Paper IV to disentangle the oxygen- and carbon-rich evolved AGB stars and the intersecting region that covers all six of the Cycle 11 observations. We have compared the LPVs detected in these intersection regions to the results of Paper II (Table 7) to understand how additional epochs have

identified high-confidence variables. Paper II identified 2σ and 3σ variables using two epochs of data. This survey confirmed a subset of those variables (Table 7). Varying spatial coverage between epochs prevented all of the Paper II variables from being confirmed. However, the increase in the number of epochs in some regions resulted in the discovery of new variables (from 2 to 46 per galaxy) that were not identified in Paper II. Given our spatially and temporally uneven coverage, the variable stars we confirm here are likely a small subset of the total variable population in each galaxy.

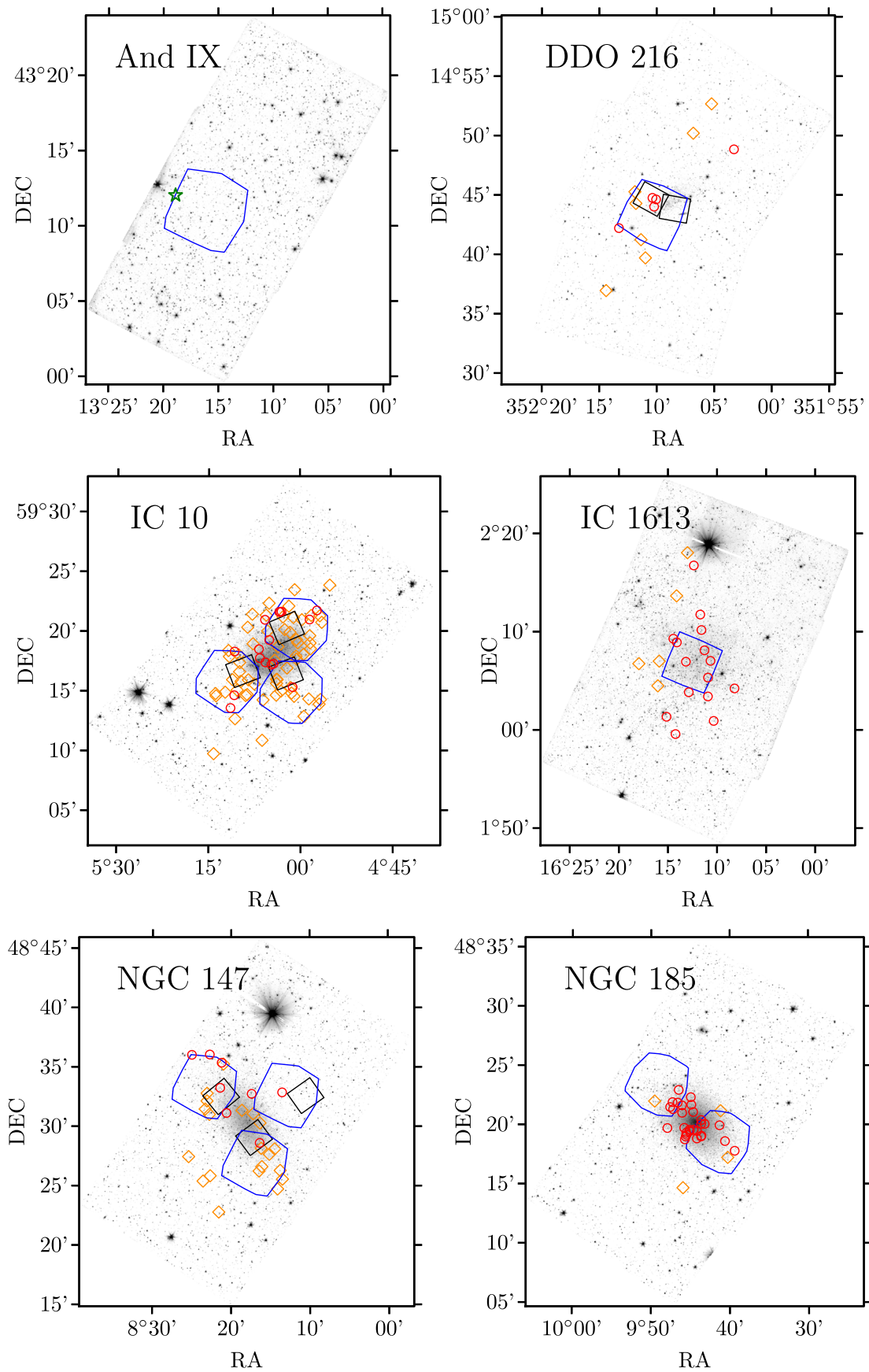


Figure 15. *Spitzer* images of the DUSTiNGS galaxies showing the spatial distribution of the high-confidence (red) and low-confidence (orange) variables, the footprint of the *Hubble* observations (black), and the intersection region that is covered by all six of the Cycle 11 DUSTiNGS supplementary observations (blue). The source And IX 46835 is shown with a green star.

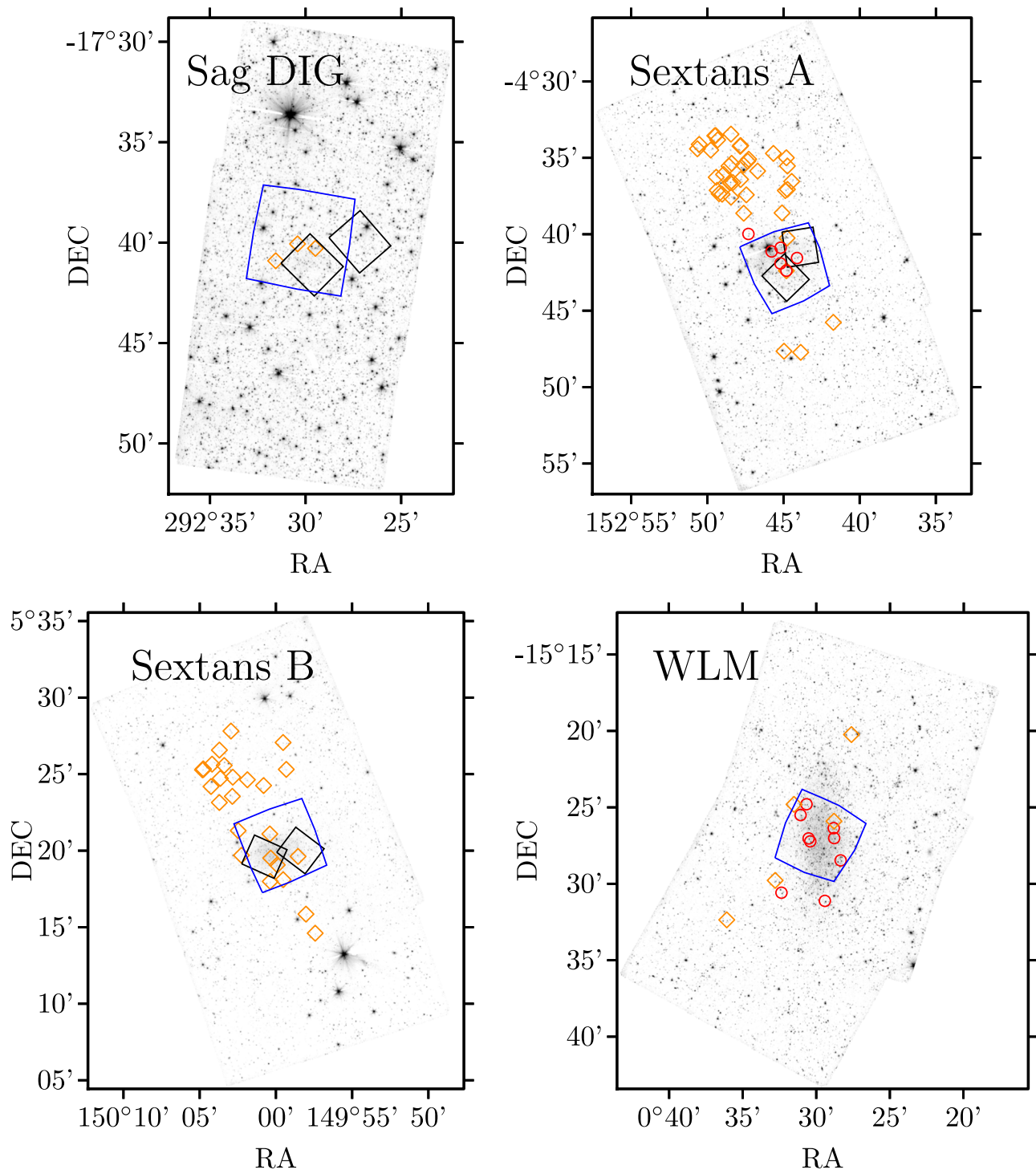


Figure 15. (Continued.)



Table 7
DUSTiNGS Results That Were Covered in Every Epoch of the Cycle 11 DUSTiNGS Supplementary Data

Galaxy	RF	IEs	UF	LPV 5000+	Paper II 2 σ x-AGBs	Paper II 3 σ x-AGBs	3 σ x-AGBs Detected in This Work
And IX	0	0	0	0	0	2	...
DDO 216	3	1	2	0	0	5	60%
IC 10	10	31	16	2	11	122	8%
IC 1613	5	0	0	0	1	10	50%
NGC 147	5	10	1	0	2	36	13%
NGC 185	16	2	0	0	2	28	57%
Sag DIG	0	3	0	0	0	5	...
Sextans A	5	1	1	0	0	21	23%
Sextans B	0	3	4	0	2	19	...
WLM	7	0	1	1	1	18	38%
Total	51	266	19%

Note. Here we list a subset of the results of the light-curve fitting that lie in the regions covered by all epochs in the Cycle 11 DUSTiNGS supplementary data (shown in blue in Figure 15). Also shown are the Paper II x-AGB stars that were also found in those regions and the percentage of those that were confirmed in this work.

The LPVs detected outside of these regions have sporadic temporal coverage and poorly constrained light curves, with the exception of a few sources with additional archival data. There is also a high number of low-confidence variables in Sextans A and Sextans B above the intersection region. This is due to a higher number of epochs covering these regions as opposed to in the south.

ORCID iDs

S. R. Goldman  <https://orcid.org/0000-0002-8937-3844>
M. L. Boyer  <https://orcid.org/0000-0003-4850-9589>
K. B. W. McQuinn  <https://orcid.org/0000-0001-5538-2614>
J. Th. van Loon  <https://orcid.org/0000-0002-1272-3017>
E. D. Skillman  <https://orcid.org/0000-0003-0605-8732>
R. D. Gehrz  <https://orcid.org/0000-0003-1319-4089>
O. C. Jones  <https://orcid.org/0000-0003-4870-5547>

References

- Alcock, C., Allsman, R. A., Alves, D., et al. 1997, *ApJ*, **486**, 697
Bellazzini, M., Beccari, G., Fraternali, F., et al. 2014, *A&A*, **566**, A44
Bladh, S., Höfner, S., Aringer, B., & Eriksson, K. 2015, *A&A*, **575**, A105
Blum, R. D., Mould, J. R., Olsen, K. A., et al. 2006, *AJ*, **132**, 2034
Blum, R. D., Srinivasan, S., Kemper, F., Ling, B., & Volk, K. 2014, *AJ*, **148**, 86
Boyer, M. L., McQuinn, K. B. W., Barmby, P., et al. 2015a, *ApJ*, **800**, 51
Boyer, M. L., McQuinn, K. B. W., Barmby, P., et al. 2015b, *ApJS*, **216**, 10
Boyer, M. L., McQuinn, K. B. W., Groenewegen, M. A. T., et al. 2017, *ApJ*, **851**, 152
Clement, C. M., Muzzin, A., Dufton, Q., et al. 2001, *AJ*, **122**, 2587
Dell’Aglì, F., Di Criscienzo, M., Boyer, M. L., & García-Hernández, D. A. 2016, *MNRAS*, **460**, 4230
Dell’Aglì, F., Di Criscienzo, M., García-Hernández, D. A., et al. 2019, *MNRAS*, **482**, 4733
Dell’Aglì, F., Di Criscienzo, M., Ventura, P., et al. 2018, *MNRAS*, **479**, 5035
Doherty, C. L., Gil-Pons, P., Siess, L., Lattanzio, J. C., & Lau, H. H. B. 2015, *MNRAS*, **446**, 2599
Eddington, A. S. 1913, *MNRAS*, **73**, 359
Evans, A., & Gehrz, R. D. 2012, *BASI*, **40**, 213
Fazio, G. G., Hora, J. L., Allen, L. E., et al. 2004, *ApJS*, **154**, 10
Feast, M., Whitelock, P., & Menzies, J. 2002, *MNRAS*, **329**, L7
Feast, M. W., Glass, I. S., Whitelock, P. A., & Catchpole, R. M. 1989, *MNRAS*, **241**, 375
Ferrarotti, A. S., & Gail, H.-P. 2006, *A&A*, **447**, 553
Freedman, W. L., Madore, B. F., Scowcroft, V., et al. 2011, *AJ*, **142**, 192
Gallart, C., Aparicio, A., Freedman, W. L., et al. 2004, *AJ*, **127**, 1486
Galliano, F. 2018, *MNRAS*, **476**, 1445
Gehrz, R. D., Roellig, T. L., Werner, M. W., et al. 2007, *RSci*, **78**, 011302
Gerasimović, B. P. 1928, *PNAS*, **14**, 963
Glass, I. S., Schultheis, M., Blommaert, J. A. D. L., et al. 2009, *MNRAS*, **395**, L11
Goldman, S. R., van Loon, J. Th., Gómez, J. F., et al. 2018, *MNRAS*, **473**, 3835
Goldman, S. R., van Loon, J. Th., Zijlstra, A. A., et al. 2017, *MNRAS*, **465**, 403
Gordon, K. D., Meixner, M., Meade, M. R., et al. 2011, *AJ*, **142**, 102
Hamedani Golshan, R., Javadi, A., van Loon, J. T., Khosroshahi, H., & Saremi, E. 2017, *MNRAS*, **466**, 1764
Harris, W. E. 1996, *AJ*, **112**, 1487
Hashemi, S. A., Javadi, A., & van Loon, J. T. 2019, *MNRAS*, **483**, 4751
Herwig, F. 2005, *ARA&A*, **43**, 435
Höfner, S., & Olofsson, H. 2018, *A&ARv*, **26**, 1
Huang, C. D., Riess, A. G., Hoffmann, S. L., et al. 2018, *ApJ*, **857**, 67
Hughes, S. M. G., & Wood, P. R. 1990, *AJ*, **99**, 784
Ita, Y., & Matsunaga, N. 2011, *MNRAS*, **412**, 2345
Ita, Y., Tanabé, T., Matsunaga, N., et al. 2004a, *MNRAS*, **347**, 720
Ita, Y., Tanabé, T., Matsunaga, N., et al. 2004b, *MNRAS*, **353**, 705
Javadi, A., Saberi, M., van Loon, J. T., et al. 2015, *MNRAS*, **447**, 3973
Javadi, A., van Loon, J. T., Khosroshahi, H., & Mirtorabi, M. T. 2013, *MNRAS*, **432**, 2824
Javadi, A., van Loon, J. T., Khosroshahi, H. G., et al. 2017, *MNRAS*, **464**, 2103
Javadi, A., van Loon, J. T., & Mirtorabi, M. T. 2011a, *MNRAS*, **411**, 263
Javadi, A., van Loon, J. T., & Mirtorabi, M. T. 2011b, *MNRAS*, **414**, 3394
Jones, O. C., Meixner, M., Justtanont, K., & Glasse, A. 2017, *ApJ*, **841**, 15
Karakas, A. I., & Lattanzio, J. C. 2014, *PASA*, **31**, e030
Karmalkar, V. R., Adams, S. M., Whitelock, P. A., et al. 2019, arXiv:1901.07179
Kasliwal, M. M., Bally, J., Masci, F., et al. 2017, *ApJ*, **839**, 88
Kirby, E. N., Rizzi, L., Held, E. V., et al. 2017, *ApJ*, **834**, 9
Kovács, G. 2000, *A&A*, **363**, 1
Lagadec, E., & Zijlstra, A. A. 2008, *MNRAS*, **390**, L59
Lakićević, M., van Loon, J. Th., Meixner, M., et al. 2015, *ApJ*, **799**, 50
Lebzelter, T., & Wood, P. R. 2005, *A&A*, **441**, 1117
Lee, H., Skillman, E. D., Cannon, J. M., et al. 2006, *ApJ*, **647**, 970
Liljegen, S., Höfner, S. H., Freytag, B., & Bladh, S. 2018, *A&A*, **619**, A47
Lomb, N. R. 1976, *Ap&SS*, **39**, 447
Lorenz, D., Lebzelter, T., Nowotny, W., et al. 2011, *A&A*, **532**, 78
Marigo, P., Girardi, L., Bressan, A., et al. 2008, *A&A*, **482**, 883
Marigo, P., Girardi, L., Bressan, A., et al. 2017, *ApJ*, **835**, 77
Mateo, M. 1998, *ARA&A*, **36**, 435
Mathias, P., Aurière, M., López Ariste, A., et al. 2018, *A&A*, **615**, A116
McConnachie, A. W. 2012, *AJ*, **144**, 4
McDonald, I., Boyer, M. L., Groenewegen, M. A. T., et al. 2019, *MNRAS*, **484**, L85
McDonald, I., Boyer, M. L., van Loon, J. Th., et al. 2011, *ApJS*, **193**, 23
McDonald, I., De Beck, E., Zijlstra, A. A., & Lagadec, E. 2018, *MNRAS*, **481**, 4984
McDonald, I., & Trabucchi, M. 2019, arXiv:1901.06325
McDonald, I., van Loon, J. T., Dupree, A. K., & Boyer, M. L. 2010, *MNRAS*, **405**, 1711
McDonald, I., Zijlstra, A. A., Sloan, G. C., et al. 2014, *MNRAS*, **439**, 2618
McQuinn, K. B. W., Skillman, E. D., Berg, D., et al. 2013, *AJ*, **146**, 145

- McQuinn, K. B. W., Woodward, C. E., Willner, S. P., et al. 2007, *ApJ*, **664**, 850
- Meixner, M., Gordon, K. D., Indebetouw, R., et al. 2006, *AJ*, **132**, 2268
- Menzies, J., Feast, M., Whitelock, P., et al. 2008, *MNRAS*, **385**, 1045
- Menzies, J. W., Feast, M. W., Whitelock, P. A., & Matsunaga, N. 2011, *MNRAS*, **414**, 3492
- Menzies, J. W., Whitelock, P. A., & Feast, M. W. 2015, *MNRAS*, **452**, 910
- Menzies, J. W., Whitelock, P. A., Feast, M. W., & Matsunaga, N. 2010, *MNRAS*, **406**, 86
- Momany, Y., Held, E. V., Saviane, I., & Rizzi, L. 2002, *A&A*, **384**, 393
- Nanni, A., Bressan, A., Marigo, P., & Girardi, L. 2013, *MNRAS*, **434**, 2390
- Nanni, A., Bressan, A., Marigo, P., & Girardi, L. 2014, *MNRAS*, **438**, 2328
- Nicholls, C. P., Wood, P. R., Cioni, M. R. L., & Soszyński, I. 2009, *MNRAS*, **399**, 2063
- Poudel, S., Kulkarni, V. P., Morrison, S., et al. 2017, *MNRAS*, **473**, 3559
- Rafelski, M., Wolfe, A. M., Prochaska, J. X., Neeleman, M., & Mendez, A. J. 2012, *ApJ*, **755**, 89
- Riebel, D., Boyer, M. L., Srinivasan, S., et al. 2015, *ApJ*, **807**, 1
- Riebel, D., Meixner, M., Fraser, O., et al. 2010, *ApJ*, **723**, 1195
- Rieke, G. H., Wright, G. S., Böker, T., et al. 2015, *PASP*, **127**, 584
- Salvatier, J., Wiecki, T. V., & Fonnesbeck, C. 2016, *PyMC3: Python Probabilistic Programming Framework*, Astrophysics Source Code Library, ascl:1610.016
- Saviane, I., Rizzi, L., Held, E. V., Bresolin, F., & Momany, Y. 2002, *A&A*, **390**, 59
- Scargle, J. D. 1982, *ApJ*, **263**, 835
- Scowcroft, V., Freedman, W. L., Madore, B. F., et al. 2011, *ApJ*, **743**, 76
- Skillman, E. D., Terlevich, R., & Melnick, J. 1989, *MNRAS*, **240**, 563
- Sloan, G. C., Kraemer, K. E., McDonald, I., et al. 2016, *ApJ*, **826**, 44
- Sloan, G. C., Matsuura, M., Lagarde, E., et al. 2012, *ApJ*, **752**, 140
- Sloan, G. C., Matsunaga, N., Matsuura, M., et al. 2010, *ApJ*, **719**, 1274
- Sloan, G. C., Matsuura, M., Zijlstra, A. A., et al. 2009, *Sci*, **323**, 353
- Soszyński, I., Udalski, A., Szymański, M. K., et al. 2009, *AcA*, **59**, 239
- Stetson, P. B. 1987, *PASP*, **99**, 191
- Temim, T., Dwek, E., Tchernyshyov, K., et al. 2015, *ApJ*, **799**, 158
- Trabucchi, M., Wood, P. R., Montalbán, J., et al. 2017, *ApJ*, **847**, 139
- Trabucchi, M., Wood, P. R., Montalbán, J., et al. 2018, *MNRAS*, **482**, 929
- Udalski, A., Kubiak, M., & Szymański, M. 1997, *AcA*, **47**, 319
- van Loon, J. T. 2000, *A&A*, **354**, 125
- van Loon, J. T. 2006, in ASP Conf. Ser. 353, *Stellar Evolution at Low Metallicity: Mass Loss, Explosions, Cosmology*, ed. H. J. G. L. M. Lamers et al. (San Francisco, CA: ASP), 211
- van Loon, J. T., Marshall, J. R., & Zijlstra, A. A. 2005, *A&A*, **442**, 597
- VanderPlas, J. T. 2018, *ApJS*, **236**, 16
- Weisz, D. R., Dolphin, A. E., Skillman, E. D., et al. 2014, *ApJ*, **789**, 147
- Werner, M. W., Roellig, T. L., Low, F. J., et al. 2004, *ApJS*, **154**, 1
- Whitelock, P. A. 2012, *Ap&SS*, **341**, 123
- Whitelock, P. A., Feast, M. W., Marang, F., & Groenewegen, M. A. T. 2006, *MNRAS*, **369**, 751
- Whitelock, P. A., Kasliwal, M., & Boyer, M. 2017, in *European Physical Journal Web of Conf. 152, Wide-Field Variability Surveys: A 21st Century Perspective*, ed. M. Catalan & W. Gieren, 1009, arXiv:1702.06797
- Whitelock, P. A., Menzies, J. W., Feast, M. W., et al. 2009, *MNRAS*, **394**, 795
- Whitelock, P. A., Menzies, J. W., Feast, M. W., & Marigo, P. 2018, *MNRAS*, **473**, 173
- Wood, P. R. 2015, *MNRAS*, **448**, 3829
- Wood, P. R., Alcock, C., Allsman, R. A., et al. 1999, in *IAU Symp. 191, Asymptotic Giant Branch Stars*, ed. T. Le Bertre, A. Lèbre, & C. Waelkens (Cambridge: Cambridge Univ. Press), 151
- Yuan, W., Macri, L. M., Javadi, A., Lin, Z., & Huang, J. Z. 2018, *AJ*, **156**, 112
- Zhukovska, S., Gail, H. P., & Trieloff, M. 2008, *A&A*, **479**, 453